

ALMA OBSERVATIONS OF NEARBY LUMINOUS INFRARED GALAXIES WITH VARIOUS AGN ENERGETIC CONTRIBUTIONS USING DENSE GAS TRACERS

MASATOSHI IMANISHI^{1,2}

Subaru Telescope, 650 North A'ohoku Place, Hilo, Hawaii, 96720, U.S.A.

AND

KOUCIHIRO NAKANISHI^{1,2}

Joint ALMA Observatory, Alonso de Córdova 3107, Vitacura 763-0355, Santiago de Chile

AJ

ABSTRACT

We present the results of our ALMA Cycle 0 observations, using HCN/HCO⁺/HNC J=4–3 lines, of six nearby luminous infrared galaxies with various energetic contributions from active galactic nuclei (AGNs) estimated from previous infrared spectroscopy. These lines are very effective for probing the physical properties of high-density molecular gas around the hidden energy sources in the nuclear regions of these galaxies. We find that HCN to HCO⁺ J=4–3 flux ratios tend to be higher in AGN-important galaxies than in starburst-dominated regions, as was seen at the J=1–0 transition, while there is no clear difference in the HCN-to-HNC J=4–3 flux ratios among observed sources. A galaxy with a starburst-type infrared spectral shape and very large molecular line widths shows a high HCN-to-HCO⁺ J=4–3 flux ratio, which could be due to turbulence-induced heating. We propose that enhanced HCN J=4–3 emission relative to HCO⁺ J=4–3 could be used to detect more energetic activity than normal starbursts, including deeply buried AGNs, in dusty galaxy populations.

Subject headings: galaxies: active — galaxies: nuclei — quasars: general — galaxies: Seyfert — galaxies: starburst — submillimeter: galaxies

1. INTRODUCTION

Luminous infrared galaxies (LIRGs) and ultraluminous infrared galaxies (ULIRGs) emit very strong infrared (8–1000 μm) radiation with luminosity of $L_{\text{IR}} > 10^{11} L_{\odot}$ and $> 10^{12} L_{\odot}$, respectively (Sanders & Mirabel 1996). The strong infrared emission indicates that (U)LIRGs contain powerful energy sources hidden behind dust. The dust-obscured energy sources of (U)LIRGs may be either nuclear fusion reactions inside rapidly formed stars (starburst) and/or radiative energy generation by an accreting compact supermassive black hole (SMBH) with mass of $> 10^6 M_{\odot}$ (active galactic nucleus; AGN). Understanding the (U)LIRG's hidden energy sources is indispensable to clarify the nature of the (U)LIRG population. However, this is not easy because the powerful compact nuclear starbursts found in the bulk of (U)LIRGs are not clearly distinguishable from very compact AGN activity based on imaging observations alone at the distance of many (U)LIRGs of interest. Since (U)LIRGs are the dominant population at $z > 1$ in terms of the cosmic infrared radiation density (Caputi et al. 2007; Goto et al. 2010; Magnelli et al. 2011; Murphy et al. 2011), establishing a reliable method to differentiate the hidden energy sources of dusty (U)LIRG populations is useful to unravel the history of star formation and SMBH mass growth in the dust-obscured side of galaxy formation in the early universe.

If AGNs are surrounded by toroidally distributed (torus-shaped) dusty medium, the so-called narrow line

regions, which are photoionized by AGN radiation, should develop at 10–1000 pc along the torus axis, above the torus scale height (Antonucci 1993). Since emission from the narrow line regions in AGNs is visible from all directions, such classical AGNs obscured by torus-shaped dusty medium are classified optically as Seyfert 2s, and are therefore distinguishable from starbursts through optical spectroscopic classification, based on optical emission line flux ratios (Veilleux & Osterbrock 1987; Kewley et al. 2001; Kauffmann et al. 2003). However, (U)LIRGs are major mergers of gas-rich galaxies and have large amounts of concentrated molecular gas and dust in their nuclei (Sanders & Mirabel 1996). The putative compact AGNs in (U)LIRG nuclei can be easily obscured by dust and gas in virtually all directions in the inner part of the surrounding obscuring material. Hence, optical detection of AGN signatures becomes very difficult, because the narrow line regions can be significantly underdeveloped. Understanding the energetic importance of such optically elusive *buried* AGNs is crucial to clarify the true nature of the (U)LIRG population, as well as the SMBH mass growth process during gas-rich galaxy mergers (Hopkins et al. 2006).

To investigate buried AGNs in dusty (U)LIRG nuclei, it is essential to perform observations at wavelengths where dust extinction effects are small. The infrared 2.5–35 μm band is one such region. Systematic infrared 2.5–35 μm spectroscopy of nearby (U)LIRGs has allowed elucidation of the energetic role of buried AGNs in a quantitative manner (Imanishi et al. 2006a; Imanishi 2006; Imanishi et al. 2007a, 2008, 2010a,b; Imanishi 2009; Nardini et al. 2008, 2009, 2010; Veilleux et al. 2009; Lee et al. 2012). However, our understanding of distant ($z > 1$) (U)LIRGs is incomplete, because at $z > 1$, application of this infrared spectroscopy is limited to infrared 24 μm

Electronic address: masa.imanishi@nao.ac.jp

¹ National Astronomical Observatory of Japan, 2-21-1 Osawa, Mitaka, Tokyo 181-8588

² Department of Astronomy, School of Science, Graduate University for Advanced Studies (SOKENDAI), Mitaka, Tokyo 181-8588

very bright sources only (Weedman et al. 2006; Sajina et al. 2007; Dasyra et al. 2009), which are strongly biased toward AGNs (Papovich et al. 2007; Donley et al. 2008; Lee et al. 2010). No significant progress is expected until the SPICA satellite, which has high sensitivity in the infrared 10–200 μm range, becomes operational after 2020 (Nakagawa et al. 2012).

Starbursts (nuclear fusion) and buried AGNs (mass accretion onto SMBHs) have very different energy generation mechanisms. First, the radiative energy generation efficiency of a nuclear fusion reaction in a starburst is only $\sim 0.7\%$ of Mc^2 (where M is the mass of material used in the nuclear fusion reaction, and c is the speed of light). Thus, the emission surface brightness of a starburst region is modest and has both observational (Werner et al. 1976; Soifer et al. 2000) and theoretical (Thompson et al. 2005) upper limits of $\sim 10^{13}L_{\odot} \text{ kpc}^{-2}$. An AGN, however, achieves high radiative energy generation efficiency (6%–42% of Mc^2 , where M is the mass of accreting material) (Bardeen 1970; Thorne 1974), and can produce high luminosity from a very compact region. A high emission surface brightness with $>10^{13}L_{\odot} \text{ kpc}^{-2}$ (Soifer et al. 2000) can be achieved in an AGN, and a large amount of dust in the close vicinity of the AGN can be heated to high temperatures (several 100 K). Second, while UV is the dominant energetic radiation in a starburst, an AGN emits strong X-rays in addition to UV radiation (Ranalli et al. 2003; Shang et al. 2011). Since it is predicted that these AGN-origin high dust temperatures and strong X-ray irradiation cause different chemical reactions for molecules compared to starbursts (Meijerink & Spaans 2005; Lintott & Viti 2006; Harada et al. 2010, 2013), different flux ratios of molecular rotational J-transition lines could be observed between AGNs and starbursts in the (sub)millimeter wavelength range. This difference may be used to distinguish the hidden energy sources of dusty galaxy populations, because of the negligible effects of dust extinction at (sub)millimeter wavelengths.

Observational results of possibly different effects and feedback to the surrounding molecular gas between AGNs and starbursts have been reported, based on CO, HCN, HCO^+ , and HNC rotational J-transition line observations of nearby bright starburst and Seyfert galaxies (modest luminosity AGNs) (Kohno 2005; Perez-Beaupuits et al. 2007; Krips et al. 2008; Costagliola et al. 2011). For example, it has been argued that AGNs show HCN J=1–0 (rotational transition) flux enhancement, relative to HCO^+ J=1–0 (Kohno 2005; Krips et al. 2008). However, the interpretation of these results is controversial, because observational data are sparse for sources for which the energetic contributions of AGNs are quantitatively well-constrained. In nearby Seyfert galaxies, modestly luminous AGNs are surrounded by starburst activity in nuclear regions (Imanishi 2002, 2003; Rodriguez-Ardila & Viegas 2003; Imanishi & Wada 2004; Oi et al. 2010) and circum-nuclear regions in host galaxies (Clavel et al. 2000; Watabe et al. 2008; Woo et al. 2012). The AGN and starburst energetic contributions can vary markedly depending on the aperture size employed. Hence, a comparison among various observations at different wavelengths with different aperture sizes is not straightforward, which makes the discussion highly uncertain.

Nearby ($z < 0.4$) ULIRGs are energetically dominated by nuclear compact ($<$ a few 100 pc in physical scale, or $<0''.5$ at $z > 0.04$) energy sources (Soifer et al. 2000; Imanishi et al. 2011a), so that various observational data at different wavelengths (with different aperture sizes) must reflect the properties of nuclear emission, with minimum contamination from spatially extended ($>$ kpc scale) star formation activity in host galaxies. The relative energetic contributions from starbursts and AGNs have also been estimated *quantitatively* and *consistently* for many nearby ULIRG nuclei through systematic infrared 2.5–35 μm spectroscopy (Veilleux et al. 2009; Imanishi et al. 2010a,b; Nardini et al. 2010). Nearby ULIRGs are thus excellent laboratories in which to create a template of molecular line flux ratio from AGNs and starbursts, and to scrutinize AGN effects and feedback on molecular rotational (J)-transition line flux ratios in a quantitatively reliable manner.

Since ULIRG nuclear regions are dominated by dense molecular gas (Gao & Solomon 2004a), observations with molecular lines with high critical densities (e.g., HCN, HCO^+ , HNC), rather than the widely used low-J CO lines, are needed to properly probe AGN effects in ULIRG nuclei. Pre-ALMA interferometric observations using HCN and HCO^+ J=1–0 were performed for nearby bright ULIRGs at $z < 0.06$ to probe their nuclear molecular gas properties. It was found that ULIRG nuclei classified as AGN-important based on infrared spectra tend to show higher HCN-to- HCO^+ J=1–0 flux ratios than starburst-classified nuclei (Imanishi et al. 2004, 2006b; Imanishi & Nakanishi 2006; Imanishi et al. 2007b, 2009), supporting the suggestion that enhanced HCN emission can be used to detect AGNs. With the advent of highly sensitive ALMA, this study is in principle applicable to fainter sources. However, at $z > 0.06$, these J=1–0 lines will be redshifted beyond the frequency (wavelength) coverage of ALMA band 3, and hence will not be observable with the current specification of ALMA. It is particularly important to establish an energy diagnostic method using higher J-transition lines at higher frequencies (shorter wavelengths), which can be applied to distant ULIRGs using ALMA.

For nearby sources, J=4–3 and J=3–2 transition lines of HCN, HCO^+ , and HNC were observable in ALMA band 7 (275–373 GHz) and 6 (211–275 GHz), respectively, during ALMA Cycle 0, while J=2–1 lines were not. Earth’s atmospheric background emission is smaller in band 6 than in band 7, and so observations in band 6 to cover J=3–2 transition lines of HCN, HCO^+ , and HNC are easier. However, if excitation is thermal at up to J=4–3, the flux of J=4–3 is higher by a factor of 16/9 than that of J=3–2, largely compensating for the higher atmospheric background noise of Earth at J=4–3 in band 7. Given reasonable assumptions about the observing conditions, the ALMA sensitivity calculator showed that the required on source exposure times for the same detection significance (same S/N ratio) were similar between the J=3–2 and J=4–3 lines of HCN, HCO^+ , and HNC, if the excitation is thermal at up to J=4–3. Given that the J=4–3 line energy diagnostic is applicable to higher redshift sources than that of J=3–2 using ALMA, we selected J=4–3 line as our initial choice, with the caution that the J=3–2 line could be better for detection if the excitation is significantly sub-thermal.

We performed HCN J=4–3 (rest-frame frequency $\nu_{\text{rest}} = 354.505$ GHz), HCO⁺ J=4–3 ($\nu_{\text{rest}} = 356.734$ GHz), and HNC J=4–3 ($\nu_{\text{rest}} = 362.630$ GHz) observations of nearby ULIRGs with well-calibrated energy sources. Since HCN, HCO⁺, and HNC have similar dipole moments ($\mu = 3.0, 3.9,$ and 3.1 Debye, respectively) and similar frequencies for individual J transitions, it is likely that similar dense gas phases are probed by these molecular lines, making the interpretation straightforward. Throughout this paper, we adopt $H_0 = 71 \text{ km s}^{-1} \text{ Mpc}^{-1}$, $\Omega_M = 0.27$, and $\Omega_\Lambda = 0.73$ (Komatsu et al. 2009).

2. TARGETS

Our primary interest is to determine whether AGN-important galaxies display noticeably different molecular line flux ratios from starburst-dominated galaxies. Therefore, we targeted galaxies for which the energetic contributions from AGNs are reasonably well estimated through infrared spectroscopy and/or other observations. Since we expected that the ALMA molecular gas observations of many nearby well-studied starburst galaxies and Galactic active star-forming regions would be performed with other programs, we mainly selected AGN-dominated ULIRGs as the first priority to probe the molecular line flux ratios from almost pure AGNs.

AGN and starburst activity generally coexist in galaxies, so it is not easy to find such pure AGNs. The SMBH and spheroidal stellar mass correlation (Magorrian et al. 1998; Ferrarese & Merritt 2000; Gültekin et al. 2009; McConnell & Ma 2013) means that the SMBH to stellar mass ratio does not change markedly among different galaxies. However, the *luminosity* ratio between AGNs and starbursts can change depending on the mass accretion rate onto SMBHs. Galaxies containing highly mass-accreting SMBHs have relatively high AGN contributions to the total energy budgets, and hence are good targets to investigate the effects of AGNs on molecular line flux ratios. The energetic importance of AGNs increases with the galaxy infrared luminosity. Buried AGN-dominated sources with no detectable starburst activity were found in ULIRGs with $L_{\text{IR}} > 10^{12} L_\odot$, (Veilleux et al. 2009; Imanishi 2009; Imanishi et al. 2010a; Nardini et al. 2010; Imanishi et al. 2010b). These sources were excellent targets for our investigation of AGN effects on molecular line emission. While many PG QSOs (Schmidt & Green 1983) (higher luminosity type-1 unobscured AGN populations than Seyfert galaxies), are present at similar distances to nearby ULIRGs ($z=0.05\text{--}0.4$), and their luminosities largely come from AGNs (Veilleux et al. 2009), starbursts are still often detectable in their nuclear regions (with similar nuclear starburst to AGN luminosity ratios to Seyfert galaxies; Imanishi et al. 2011b), as well as in spatially extended host galaxies (Schweitzer et al. 2006; Netzer et al. 2007; Shi et al. 2007; Veilleux et al. 2009; Watabe et al. 2009). Although some PG QSOs do not show detectable starburst activity, we chose buried AGN-dominated ULIRGs for the following reasons. First, for the same AGN luminosity, we can expect higher molecular emission line fluxes in buried AGNs surrounded by a large amount of molecular gas and dust than in type-1 unobscured AGNs with a smaller dust/gas covering factor. Hence, higher S/N ratios can be obtained and more distant sources can be observed for buried AGNs than for type-1 unobscured AGNs. Sec-

ond, the primary energy sources of type-1 unobscured AGNs can be investigated through optical spectroscopic classification (Veilleux & Osterbrock 1987; Kewley et al. 2001; Kauffmann et al. 2003). There is no strong need to observe such unobscured AGNs in the (sub)millimeter wavelength range just for the purposes of energy diagnostics.

Among buried AGN-dominated ULIRGs with no detectable starburst activity, we first picked up those with the highest expected HCN fluxes. This allowed us to obtain the highest quality spectra with the limited capabilities of ALMA Cycle 0. Given the correlation between infrared and HCN J=1–0 line luminosity in galaxies (Gao & Solomon 2004a), higher HCN J=1–0 emission flux is expected in a galaxy with higher infrared flux. IRAS 08572+3915, 12127–1412, and 00183–7111 were selected as our buried AGN-dominated ULIRG sample.

IRAS 08572+3915 ($z = 0.058$) is a ULIRG ($L_{\text{IR}} \sim 10^{12.1} L_\odot$) (Table 1) classified optically as a LINER (Veilleux et al. 1999) or a Seyfert 2 in some combination of optical emission lines (Yuan et al. 2010). It consists of two merging nuclei with $\sim 5''$ separation (NW and SE) (Scoville et al. 2000; Kim et al. 2002; Imanishi & Saito 2014). The NW nucleus (IRAS 08572+3915 NW) is one of the strongest buried AGN candidates in the local universe, because (1) the energy source is suggested to be very compact and is more centrally concentrated than the nuclear dust, as is expected for a buried AGN (Dudley & Wynn-Williams 1997; Soifer et al. 2000; Imanishi et al. 2006a, 2007a), and (2) the infrared polycyclic aromatic hydrocarbons (PAH) emission (a good starburst indicator) is extremely weak (Imanishi & Dudley 2000; Imanishi et al. 2006a; Spoon et al. 2006; Armus et al. 2007; Imanishi et al. 2007a; Veilleux et al. 2009; Nardini et al. 2010). The detection of many high-J transition CO absorption lines in the infrared spectrum is also suggestive of the presence of a luminous AGN (Shirahata et al. 2013).

IRAS 12127–1412 ($z = 0.133$) is our second buried AGN-dominated ULIRG sample ($L_{\text{IR}} \sim 10^{12.1} L_\odot$) (Table 1). It consists of two main nuclei (NE and SW) with a separation of $\sim 10''$ (Kim et al. 2002), and is classified optically as a non-Seyfert (LINER or HII-region) (Veilleux et al. 1999; Yuan et al. 2010). The NE nucleus is brighter in the infrared (Kim et al. 2002; Imanishi & Saito 2014), and is diagnosed as buried AGN-dominated based on the suggested compact energy source, which is more centrally concentrated than the nuclear dust, and (2) non-detectable starburst-originated PAH emission features in the infrared (Imanishi et al. 2006a, 2007a; Veilleux et al. 2009; Imanishi et al. 2010a; Nardini et al. 2010).

IRAS 00183–7111 ($z = 0.327$), which is classified optically as a LINER (Armus et al. 1989), is a third almost pure buried AGN candidate, based on its buried AGN type infrared spectral shape (Spoon et al. 2004, 2009; Imanishi et al. 2010a). X-ray observations also support the AGN-dominant scenario for this ULIRG (Nandra & Iwasawa 2007). Although its distance is greater than the former two buried AGN candidates, the high infrared luminosity ($L_{\text{IR}} \sim 10^{12.9} L_\odot$) keeps the infrared *flux* relatively high, making this a good target for our study.

As a comparison of molecular emission line flux ratios for these buried AGN-dominated ULIRGs, we selected

a starburst-dominated galaxy. Since spatially extended emission with $>6''$ could be missed by ALMA Cycle 0 observations, we chose the nuclear compact starburst-dominated galaxy NGC 1614. NGC 1614 has infrared luminosity with only $L_{\text{IR}} \sim 10^{11.6} L_{\odot}$ (Table 1), and so is not classified as an ULIRG. Our ALMA Cycle 0 observational results of NGC 1614 were published previously by Imanishi & Nakanishi (2013a), and detailed descriptions about the properties of NGC 1614 are found in that paper.

Since starbursts in ULIRGs could be more powerful per unit volume than those in LIRGs, molecular gas excitation could differ, and so molecular line flux ratios from starburst galaxies could vary, depending on the infrared luminosity. Therefore, we also included an ULIRG with a starburst-type infrared spectral shape. Among many such ULIRGs (Imanishi et al. 2007a; Veilleux et al. 2009; Imanishi et al. 2010a), to achieve the highest S/N ratios with a given ALMA Cycle 0 observing time, we searched for sources with high infrared fluxes, at declinations between -40° and 0° , which were best observable from the ALMA site in Chile. We picked up IRAS 22491–1808 ($z=0.076$; $L_{\text{IR}} \sim 10^{12.1} L_{\odot}$) as our ALMA Cycle 0 starburst ULIRG sample. IRAS 22491–1808 has an infrared spectrum dominated by large equivalent width PAH emission features, suggesting that the *observed* infrared flux is dominated by starburst activity (Imanishi et al. 2007a; Veilleux et al. 2009; Imanishi et al. 2010a). However, the starburst-originated PAH emission to infrared luminosity ratios are a factor of 3–8 smaller than the typical ratios for less-infrared-luminous starburst-dominated galaxies for the $3.3 \mu\text{m}$, $6.2 \mu\text{m}$, and $11.3 \mu\text{m}$ features (Imanishi et al. 2007a, 2010a). This leaves room for an additional energy source beyond the modestly obscured detected starburst activity (i.e., a deeply buried AGN that does not show PAH emission and/or an extremely highly obscured starburst whose PAH emission is highly flux attenuated). This uncertainty is unavoidable for the majority of starburst-classified ULIRGs based on infrared spectra, which show deficiency in PAH to infrared luminosity ratios. Based on the infrared spectrum of IRAS 22491–1808 at $\lambda > 5 \mu\text{m}$, Veilleux et al. (2009) classified this ULIRG as starburst-dominated, with the energetic contribution from a buried AGN of $\sim 18\%$, but Nardini et al. (2010) failed to determine the relative energetic contribution between the starburst and the AGN.

In addition to these five sources, we added a buried AGN *significant* galaxy, where both AGN and starburst energetically contribute to roughly half of the total luminosity. We did this to determine whether such a source shows molecular line flux ratios between AGN-dominated and starburst-dominated galaxies. For this class, we chose IRAS 20551–4250 ($z=0.043$, $L_{\text{IR}} \sim 10^{12.0} L_{\odot}$). We refer readers to Imanishi & Nakanishi (2013b) for the details of our ALMA Cycle 0 results of IRAS 20551–4250.

In total, six sources with various AGN energetic contributions were observed. Table 1 presents a summary of their basic properties.

3. OBSERVATIONS AND DATA ANALYSIS

All observations were made during ALMA Cycle 0 within the program 2011.0.00020.S (PI = M. Imanishi). Observation details of NGC 1614 and IRAS 20551–4250

are presented in Imanishi & Nakanishi (2013a,b), and are not repeated here. Table 2 describes the observation details for the remaining four ULIRGs. HCN J=4–3 ($\nu_{\text{rest}} = 354.505 \text{ GHz}$) and HCO^+ J=4–3 ($\nu_{\text{rest}} = 356.734 \text{ GHz}$) lines were simultaneously observable with ALMA, but we needed separate observations to cover the HNC J=4–3 line ($\nu_{\text{rest}} = 362.630 \text{ GHz}$). Band 7 was used for all sources except IRAS 00183–7111 ($z = 0.327$), for which band 6 was used due to its high redshift. We adopted the widest 1.875 GHz band width mode. In ALMA Cycle 0, four different frequencies can be configured with some restrictions. HCN and HCO^+ J=4–3 lines were covered by two separate correlator spectral windows. The other two spectral windows were also used to measure the continuum flux levels. For HNC J=4–3 observations, the HNC line was covered with one spectral window, and an additional spectral window was used to probe the continuum emission. The central frequencies used in each correlator spectral window are summarized in Table 3. According to the observing log of ALMA Cycle 0, observations of IRAS 08572+3915 at the HNC J=4–3 line were performed, but the data were not provided to us because they did not pass the most basic quality assessment checks.

We started data analysis from calibrated data provided by the Joint ALMA Observatory, using CASA, except the IRAS 22491–1808 HNC data, for which the phase center position of the phase calibrator (J2258–279) on the UV data delivered to us was incorrect and was slightly shifted by $\sim 1''$. We corrected for the phase center by using the CASA task ‘fixvis’ and re-calibrated the IRAS 22491–1808 HNC data. We first checked the visibility plots to determine whether the signatures of targeted emission lines were recognizable. For most of the detected emission lines, the presence of the lines was evident in the visibility plot. We then selected channels that were free from strong emission lines to estimate the continuum flux level. As will be discussed in the following section, in addition to the targeted HCN, HCO^+ , and HNC J=4–3 emission lines, clear signatures of other emission lines were detected in a few sources in the spectral windows originally set to measure the continuum emission. Those channels that were affected by strong emission lines were excluded from the continuum extraction. We then subtracted the estimated continuum emission from the spectra, and performed the task “clean” for continuum-subtracted molecular line data, as well as for the continuum data themselves. To create spectra, we binned 40 channels ($17\text{--}18 \text{ km s}^{-1}$ in band 7 and $22\text{--}23 \text{ km s}^{-1}$ in band 6). For spatial binning, we employed $0''.3 \text{ pixel}^{-1}$ or $0''.1 \text{ pixel}^{-1}$, depending on the beam size of the obtained data. The resulting beam sizes of continuum and individual molecular line data of the observed sources are shown in Tables 4 and 5, respectively. The energetically-dominant nuclear regions ($< a$ few 100 pc) of the observed (U)LIRGs are fully covered with our ALMA Cycle 0 data.

4. RESULTS

Our ALMA Cycle 0 observational results of NGC 1614 and IRAS 20551–4250 have been published in Imanishi & Nakanishi (2013a) and Imanishi & Nakanishi (2013b), respectively. Here, we present the results of the remaining four ULIRGs. Figure 1 shows the continuum-a

(taken with HCN and HCO⁺ J=4–3 observations) and continuum-b (taken with HNC J=4–3) maps. The continuum peak fluxes and peak coordinates are summarized in Table 4. The peak coordinates generally agree between continuum-a and -b.

The spectra at the continuum peak positions within the beam size are shown in Figure 2. Although we targeted HCN, HCO⁺, and HNC J=4–3 emission line observations, the signatures of other emission lines were seen at the rest frame frequency of $\nu_{\text{rest}} \sim 369.1$ GHz and ~ 349.4 GHz, which we ascribed to H₂S 3(2,1)–3(1,2) ($\nu_{\text{rest}} \sim 369.101$ GHz) and CH₃CN v=0 19(3)–18(3) ($\nu_{\text{rest}} \sim 349.393$ GHz) with possible contamination from CCH v=0 N=4–3 J=7/2–5/2 ($\nu_{\text{rest}} \sim 349.400$ GHz), respectively. For IRAS 12127–1412, the signature of the CS J = 7–6 line ($\nu_{\text{rest}} = 342.883$ GHz) may be present.

Figures 3, 4, 5, and 6 are integrated intensity (moment 0) maps and spectra at the continuum peak, within the beam size, of possibly detected emission lines for IRAS 08572+3915, IRAS 12127–1412, IRAS 00183–7111, and IRAS 22491–1808, respectively. In the spectra (right), the continuum level was found to be well-subtracted, so that the moment 0 maps (left) should reflect the properties of molecular emission lines rather than the residual of continuum subtraction. The peak flux values and detection significance in the moment 0 maps are summarized in Table 5. The peak coordinates of the molecular emission lines agree within 1 pixel with those of the simultaneously observed continuum-a (for HCN, HCO⁺, and H₂S) and continuum-b (for HNC and CH₃CN), with the exception of the HNC line of IRAS 00183–7111, the emission peak of which is shifted from the continuum-b peak by two pixels (0''.6) to the west. Given the beam size of 2''.2 × 1''.2 (PA = 173°; almost north-south direction) and the detection significance of 3.6 σ for the HNC moment 0 map of IRAS 00183–7111, the positional uncertainty of the HNC emission is on the order of (beam-size)/(signal-to-noise ratio) $\sim 0''.33$ in the east-west direction. The east-west offset could be larger than the statistical uncertainty, and the marginal (3.6 σ) detection of the HNC emission in IRAS 00183–7111 requires further confirmation.

To estimate the fluxes of individual molecular emission lines detected in the spectra, the lines were fitted with a Gaussian profile. The results of the Gaussian fits for individual molecular lines are summarized in Table 5. The detection significance of the possible CS J=7–6 line in IRAS 12127–1412 is $<3\sigma$ both in the moment 0 map (peak flux value relative to the rms noise level derived from the standard deviation of sky signals) and the Gaussian fit in the spectrum at the emission peak, within the beam size (Table 5). The molecular line luminosities are derived from the fluxes based on Gaussian fits, and are summarized in Table 6, where we adopted equations (1) and (3) from Solomon & Vanden Bout (2005).

Emission lines are generally detected at the expected frequency from optically derived redshifts (Table 1 and downward arrows in Figure 2). However, for IRAS 22491–1808, the detected molecular lines are appreciably offset from the expected frequency of $z = 0.076$ (Soifer et al. 1987; Kim & Sanders 1998). Our molecular line data of dense gas tracers indicate $z = 0.0776$, ~ 500 km s⁻¹ redshifted. Our molecular line redshift is comparable to the optical redshift of $z = 0.078$ derived by Strauss et al.

(1992).

For the bright HCN and HCO⁺ J=4–3 emission lines of IRAS 08572+3915 and 22491–1808, the intensity-weighted mean velocity (moment 1) and intensity-weighted velocity dispersion (moment 2) maps are shown in Figures 7 and 8, respectively. For IRAS 08572+3915, no signature of rotating motion was seen, suggesting that the dense molecular gas is very compact and not clearly spatially resolved. For IRAS 22491–1808, a rotation sign is barely seen such that the north-eastern (south-western) molecular gas is redshifted (blueshifted) with respect to the galactic nucleus. This suggests that the dense molecular gas is just spatially resolved. A noticeable feature of IRAS 22491–1808 is that HCN and HCO⁺ J=4–3 emission show considerably larger velocity dispersion (>150 km s⁻¹) in the bulk of the signal detected region than IRAS 08572+3915 ($\lesssim 100$ km s⁻¹) in the moment 2 maps.

IRAS 08572+3915 and 12127–1412 have distinct fainter secondary nuclei, SE and SW, with apparent separation of $\sim 5''$ and $\sim 10''$ from the brighter nuclei, respectively (Kim et al. 2002; Imanishi & Saito 2014). For IRAS 08572+3915 SE, we detected no significant ($>3\sigma$) emission of any of the observed molecular lines (HCN, HCO⁺, and H₂S) in the moment 0 maps within $<1''$ of the near-infrared *K*-band (2.2 μ m) peak coordinate at (09 00 25.67, +39 03 50.2) in J2000 (Kim et al. 2002). For 12127–1412 SW, significant ($>3\sigma$) emission was not seen in the moment 0 maps of HCN, HCO⁺, HNC, CH₃CN, and CS, within $<1''$ of the near-infrared *K*-band peak coordinate at (12 15 18.64, –14 29 48.8) in J2000 (Kim et al. 2002). The upper limits are $<3\sigma$ of the rms noise of individual moment 0 maps, shown in Table 5, column 5. We also searched for continuum emission within $<1''$ of the near-infrared *K*-band peak positions of IRAS 08572+3915 SE and 12127–1412 SW, but no signs were found. The upper limits are $<3\sigma$ of the rms noise, as shown in Table 4, column 5.

The vibrationally excited ($v_2=1f$) HCN J=4–3 emission line ($\nu_{\text{rest}} = 356.256$ GHz) was detected in two external galaxies, NGC 4418 (Sakamoto et al. 2010) and IRAS 20551–4250 (Imanishi & Nakanishi 2013b), both of which are thought to contain luminous buried AGNs. The expected frequency of this emission line is shown in Figure 9 for the four ULIRGs, but the line is not clearly recognizable, probably because (1) the flux of the HCN J=4–3 ($v_2=1f$) emission line itself is not high, and (2) the line width of the nearby, much stronger HCO⁺ J=4–3 emission at the vibrational ground level ($v=0$) is not as small as in NGC 4418 and IRAS 20551–4250.

5. DISCUSSION

5.1. Molecular Line Flux Ratio

Figure 10 shows a plot of the HCN-to-HCO⁺ J=4–3 and HCN-to-HNC J=4–3 flux ratios in the four ULIRGs, together with the starburst-dominated LIRG, NGC 1614 (Imanishi & Nakanishi 2013a), and the AGN-starburst composite ULIRG, IRAS 20551–4250 (Imanishi & Nakanishi 2013b). The buried AGN-dominated ULIRGs, IRAS 08572+3915, 12127–1412, and 00183–7111, show higher HCN-to-HCO⁺ flux ratios at J=4–3 than the starburst-dominated LIRG, NGC 1614. The AGN and starburst composite ULIRG, IRAS 20551–4250, is located between the buried AGN-

dominated ULIRGs and a starburst-dominated LIRG, NGC 1614, on the ordinate, as expected (§2). The starburst-classified ULIRG in the infrared spectrum, IRAS 22491–1808, shows a high HCN-to-HCO⁺ J=4–3 flux ratio, which will be discussed in the next subsection.

On the other hand, the HCN-to-HNC J=4–3 flux ratios in the abscissa are not clearly different between AGN-dominated and starburst-dominated sources. A high HCN-to-HCO⁺ J=4–3 flux ratio could be an indicator of a luminous buried AGN, and could be used to distinguish AGNs from starbursts (Imanishi et al. 2010c; Iono et al. 2013).

5.2. Interpretation

We consider three possible mechanisms for the strong HCN J=4–3 emission in AGNs, relative to HCO⁺ J=4–3. First, the HCN abundance enhancement is a natural explanation for the enhanced HCN emission. In an AGN, due to the high radiative energy generation efficiency of a mass-accreting SMBH, a larger amount of dust is heated to high temperatures (several 100 K) than in a starburst (§1). It is predicted that the HCN abundance could be enhanced, relative to HCO⁺ in high dust temperature chemistry (Harada et al. 2010). In an AGN, the HCN abundance enhancement by strong X-ray radiation is also calculated by Lintott & Viti (2006), but the HCN-to-HCO⁺ abundance ratio under X-ray irradiation is also shown to be highly model-dependent (Meijerink & Spaans 2005; Harada et al. 2013).

Second, vibrationally excited HCN emission lines were detected in AGN-hosting galaxies (Sakamoto et al. 2010; Imanishi & Nakanishi 2013b). Infrared radiative pumping (Aalto et al. 1995) by absorbing infrared $\sim 14 \mu\text{m}$ photons is the most natural mechanism for vibrational excitation, because vibrationally excited levels of HCN with $>1000 \text{ K}$ are very difficult to achieve with collisions (Sakamoto et al. 2010). Since an AGN emits infrared $14 \mu\text{m}$ continuum emission much more strongly due to AGN-heated hot dust than a starburst, this infrared radiative pumping is expected to work more effectively in an AGN. This mechanism can increase the HCN J=4–3 flux at $v=0$ through a cascade process (Rangwala et al. 2011) in comparison to collisional excitation alone. On the other hand, detection of the vibrationally excited HCO⁺ emission line has not been reported to date in any AGNs. In fact, the HCN $v_2=1-0$ absorption features at infrared $14 \mu\text{m}$ were detected in several obscured AGNs, while the HCO⁺ $v_2=1-0$ absorption features at infrared $12.1 \mu\text{m}$ were not (Lahuis et al. 2007; Veilleux et al. 2009). This may indicate that the necessary condition for the infrared radiative pumping is fulfilled more effectively for HCN than HCO⁺. Thus, this infrared radiative pumping may be the reason for the enhanced HCN J=4–3 fluxes relative to HCO⁺ J=4–3 observed in AGNs.

Third, the higher HCN-to-HCO⁺ J=4–3 flux ratios in AGNs compared to starbursts could be simply due to an excitation effect. As the critical density of HCN J=4–3 ($n_{\text{crit}} \sim 2 \times 10^7 \text{ cm}^{-3}$) is higher than that of HCO⁺ J=4–3 ($n_{\text{crit}} \sim 4 \times 10^6 \text{ cm}^{-3}$) (Meijerink et al. 2007), HCO⁺ J=4–3 is more easily excited than HCN J=4–3. The HCN-to-HCO⁺ flux ratio at J=4–3 should be lower than that at J=1–0. AGN-heated hot dust could create large amounts of hot molecular gas, and more HCN J=4–3 excitation is expected in an AGN than a starburst. This

can result in a higher HCN-to-HCO⁺ J=4–3 flux ratio in an AGN than in a starburst, even without invoking HCN abundance enhancement and/or the flux enhancement of the HCN J-transitions at $v=0$ through the infrared radiative pumping mechanism.

HCN and HNC have comparable critical densities (Meijerink et al. 2007), so their excitation is expected to be similar, as long as the same molecular gas phase is probed. The observational result that AGNs tend to show higher HCN-to-HCO⁺ J=4–3 flux ratios than starbursts but similar HCN-to-HNC J=4–3 flux ratios suggests that excitation is an important factor. That is, the larger amount of hot molecular gas in an AGN may boost HCN J=4–3 excitation, relative to HCO⁺ J=4–3, increasing the HCN-to-HCO⁺ J=4–3 flux ratios compared to a starburst, but also increase the excitation of HCN and HNC up to J=4–3 in a similar manner, without changing the HCN-to-HNC J=4–3 flux ratio.

It is also possible that the HCN abundance is enhanced relative to HCO⁺ in AGNs due to AGN-related phenomena (high dust temperature and/or strong X-ray irradiation), but that the HNC abundance is similarly enhanced. Or, it may be that the HNC J=4–3 flux at $v=0$ is also enhanced through vibrational excitation by infrared radiative pumping (Costagliola et al. 2013), in a similar way to HCN, but the HCO⁺ J=4–3 flux at $v=0$ is not.

IRAS 22491–1808 shows an infrared spectrum whose observed flux can be explained solely by starburst activity, and yet shows a high HCN-to-HCO⁺ J=4–3 flux ratio. As mentioned in §2, the presence of a buried AGN in IRAS 22491–1808 is not precluded, due to the smaller observed PAH-to-infrared luminosity ratio compared to the known starburst-dominated, less infrared-luminous galaxies. However, the direct signature of such an AGN is also lacking. A notable feature of IRAS 22491–1808 is the very large molecular line widths, with $>400\text{--}500 \text{ km s}^{-1}$ in full width at half maximum (FWHM) or $>700 \text{ km s}^{-1}$ in full width at zero intensity (FWZI) for HCN and HCO⁺ J=4–3 (Figure 6). These values are much larger than those for normal ULIRGs whose HCN and HCO⁺ line widths are typically $\sim 200\text{--}300 \text{ km s}^{-1}$ in FWHM (Gao & Solomon 2004a; Imanishi & Nakanishi 2006; Imanishi et al. 2007b), and are as high as the values of the merger-induced shock-dominated highly turbulent luminous infrared galaxy NGC 6240 (Nakanishi et al. 2005). The intensity-weighted velocity dispersion (moment 2) maps of HCN and HCO⁺ J=4–3 of IRAS 22491–1808 in Figure 8 also show much larger peak values in the bulk of galactic areas than those of IRAS 08572+3915 (Figure 7), NGC 1614 (Imanishi & Nakanishi 2013a), and IRAS 20551–4250 (Imanishi & Nakanishi 2013b). This suggests that the high-density molecular gas in IRAS 22491–1808 is particularly turbulent compared to the majority of ordinary ULIRGs. A turbulent heating mechanism (Pan & Padoan 2009) may produce large amounts of hot dust and molecular gas, and could (1) boost HCN J=4–3 excitation compared to normal starburst galaxies, (2) enhance HCN abundance under high dust temperature chemistry (see also Papadopoulos 2007), and (3) increase the effect of the infrared radiative pumping mechanism due to an increase in infrared $14 \mu\text{m}$ photons.

If sufficient amounts of hot dust and molecular gas are

created by a mechanism other than a luminous AGN, and if the enhanced HCN-to-HCO⁺ J=4–3 flux ratios are due to phenomena related to hot dust and molecular gas (i.e., increased HCN J=4–3 excitation, HCN abundance increase by hot dust chemistry, and increased efficiency of infrared radiative pumping), then the high HCN-to-HCO⁺ flux ratios could pick up not only luminous buried AGNs, but also starbursts with highly turbulent dense molecular gas. Although we obtained the molecular line data of the starburst-dominated LIRG NGC 1614 (Imanishi & Nakanishi 2013a), data on ordinary starburst-dominated ULIRGs that show usual dense molecular gas properties are lacking. Starbursts in ULIRGs could be more intense per unit volume than those in LIRGs, and could create different molecular gas excitation in such a way that HCN J=4–3 is excited to a greater extent in starbursts in ULIRGs than in the less infrared-luminous LIRGs. Molecular line data on starburst-dominated ULIRGs with normal dense molecular gas properties, if obtained in the future, would provide insight into the origin of the observed molecular line flux ratios in the highly turbulent ULIRG, IRAS 22491–1808. Observations of further well-studied (U)LIRGs are needed to better understand how molecular emission line flux ratios depend on the relative AGN and starburst energetic contributions, and other galaxy properties.

Finally, we briefly mention some other possibilities that could affect the observed molecular line flux ratios. Emission line fluxes can be reduced by dust extinction. Since the frequencies of HCN, HCO⁺, and HNC J=4–3 lines are ~ 350 GHz (~ 850 μm) in the submillimeter wavelength range, flux attenuation of these molecular lines by dust extinction is usually not significant. Matsushita et al. (2009) estimated that in the nearby well-studied ULIRG, Arp 220, dust extinction may not be negligible even in the submillimeter wavelength. Even if dust extinction at ~ 850 μm is not negligible in some of the observed (U)LIRGs, flux attenuation of HCN, HCO⁺, and HNC J=4–3 lines should be comparable, due to their similar frequencies (wavelengths). Thus, molecular line flux ratios will not change significantly by possible dust extinction in the submillimeter wavelength.

Line opacity could also have an effect on the observed molecular line fluxes. According to the wide-accepted standard scenario for molecular gas clouds in the Galaxy and external galaxies, molecular gas clouds consist of clumps with a small volume filling factor (Solomon et al. 1987). The line opacity of each clump is thought to be larger than unity for CO (Solomon et al. 1987). Emission from the other side of each clump is not completely probed from CO observations. Each clump has small molecular line widths by thermal broadening, but shows large random motion inside molecular gas clouds. Due to the velocity difference of each clump, line absorption by foreground clumps is insignificant, and clumps at the other side of the molecular gas clouds are observationally detectable. This model (the so-called mist model) can explain observed molecular gas properties very well (Solomon et al. 1987). The detailed physical parameters of each clump are observationally not well-constrained. Thus, the physical properties of each clump are assumed to be uniform inside a molecular cloud, as well as among different galaxies. The optical depths of HCN J=4–3 lines in external galaxies could be larger

than unity (Nguyen-Q-Rieu et al. 1992; Sakamoto et al. 2010; Jiang et al. 2011). Even if each clump is optically thick for HCN, as long as the uniform physical properties of each gas clump is assumed, the enhanced HCN abundance results in an increased area filling factor of HCN emission in a molecular gas cloud, and so a higher HCN J=4–3 flux from a molecular gas cloud (Imanishi et al. 2007b), not changing our previous discussion. We should note that the unconstrained physical properties of each molecular gas clump could cause the largest uncertainty about the interpretation of the observed molecular line flux ratios.

Summarizing, we regard that the proposed three scenarios (HCN abundance enhancement, infrared radiative pumping, and excitation effect) are the plausible mechanisms that could explain the variation of the observed molecular line flux ratios in (U)LIRGs with different AGN energetic contributions. If the excitation effect is important, the HCN-to-HCO⁺ flux ratios are expected to systematically decrease at higher J-transition. On the other hand, in the case of HCN abundance enhancement, the HCN-to-HCO⁺ flux ratios are not sensitive to J-transitions. Multiple J-transition molecular line observations are needed to differentiate physical mechanisms behind the observed molecular line flux ratios, with the aid of modeling (van der Tak et al. 2007). For (U)LIRGs with small molecular line widths, vibrationally-excited HCN emission lines may be detectable, by separating from the nearby, much stronger HCO⁺ emission lines at $v=0$ (Sakamoto et al. 2010; Imanishi & Nakanishi 2013b). The strengths of the detected vibrationally-excited HCN emission lines can be used to understand the general role of the infrared radiative pumping for HCN excitation in AGN-hosting (U)LIRGs.

5.3. Implications

As mentioned in §1, although the energy diagnostic method developed using the J=1–0 transition lines of HCN and HCO⁺ (Kohno 2005; Imanishi et al. 2004; Imanishi & Nakanishi 2006; Imanishi et al. 2006b, 2007b; Krips et al. 2008; Imanishi et al. 2009) is powerful, using ALMA it is applicable only to nearby galaxies with $z < 0.06$. If we can establish a reliable energy diagnostic method using a higher J transition at higher frequency (shorter wavelength), the method could potentially be applied to more distant galaxies using ALMA. Furthermore, the HCN J=4–3 lines selectively trace dense molecular gas in the nuclear regions of galaxies where AGNs are expected to be present, with even less contamination from spatially extended galaxy-wide molecular gas than at lower J-transitions. Hence, the energy diagnostic method using HCN J=4–3 could be very sensitive to the presence of luminous AGNs. These were the primary reasons why we conducted our ALMA Cycle 0 program.

In the case of thermal excitation, the flux of high-J transition lines increases proportional to the square of the frequency ($\propto \nu^2$), and so the J=4–3 flux can be 16 times higher than the J=1–0 flux. If realized, the high J=4–3 flux can keep the detection significance of molecular emission lines high, even under the higher Earth background noise at the frequency of J=4–3 compared to J=1–0. Given that the bulk of the infrared luminosity of nearby (U)LIRGs usually comes from the nuclear regions (§1), we may be able to relate the nuclear molecular gas emis-

sion properties with the IRAS-measured whole galactic infrared emission. Based on our pre-ALMA interferometric HCN J=1–0 observations of nearby (U)LIRG nuclei, the nuclear HCN J=1–0 peak flux and whole galactic infrared flux are found to be correlated (Figure 11; Left), where the actual data are summarized in Table 7. Therefore, we can empirically predict the emission peak flux of HCN J=1–0 line in the (U)LIRG nuclei from the IRAS-measured infrared flux, and can convert to the HCN J=4–3 emission peak flux assuming thermal excitation. Figure 11 (right) compares the HCN J=1–0 luminosities at (U)LIRG nuclei based on our pre-ALMA interferometric observations, with the IRAS-measured infrared luminosities from the whole galactic regions of (U)LIRGs. Our plots, particularly for the nuclei of ULIRGs with $L_{\text{IR}} \gtrsim 10^{12}L_{\odot}$, roughly follow the ratio established for ULIRGs based on single-dish telescope data (Gracia-Carpio et al. 2008), supporting the scenario that the bulk of high-density molecular gas in ULIRGs is concentrated in the energetically-dominant nuclear regions and is recovered with our pre-ALMA interferometric data with ~ 1 to several arcsec spatial resolution.

Table 8 presents a comparison of the expected HCN J=4–3 peak flux for thermal excitation with the observed peak flux. It can be seen that the HCN J=4–3 emission peak is substantially smaller than that expected from thermal excitation, indicating that HCN is sub-thermally excited at J=4–3 even in our active ULIRG sample, often hosting luminous buried AGNs. Thus, lower J transitions (J=3–2 or 2–1) may be better in terms of the detection significance of HCN J-transition line per given observing time. It is necessary to find the best J transition lines with which we can reliably and efficiently separate deeply buried AGNs from the surrounding starbursts in a dusty ULIRG population.

6. SUMMARY

We conducted HCN, HCO⁺, and HNC J=4–3 observations of nearby dusty (U)LIRGs with different levels of AGN energetic contributions to the observed infrared luminosities, in ALMA Cycle 0, to probe the physical properties of dense molecular gas around the dust-obscured energy sources in the nuclei. Six sources were observed in total, and the results of two sources had been published previously (Imanishi & Nakanishi 2013a,b). We mainly discussed the results of the remaining four sources in this paper, and made the following summary.

1. HCN, HCO⁺, HNC J=4–3 lines were significantly ($>3\sigma$) detected in most of the observed ULIRGs, suggesting the presence of a large amount of dense molecular gas that is sufficiently excited to J=4–3.
2. The three buried AGN-dominated ULIRGs, IRAS 00183–7111, 08572+3915, and 12127–1412, showed higher HCN-to-HCO⁺ J=4–3 flux ratios than the less infrared-luminous starburst-dominated galaxy, NGC 1614, supporting the previously reported trend that HCN emission is enhanced relative to HCO⁺, in AGNs compared to starbursts. We saw no clear differences in the HCN-to-HNC J=4–3 flux ratios between AGN-important ULIRGs and the starburst-dominated galaxy, NGC 1614.

3. Three possible mechanisms were proposed for the origin of the enhanced HCN J=4–3 emission relative to HCO⁺ J=4–3 in AGNs: (1) HCN abundance enhancement under high dust temperature chemistry and/or X-ray induced chemistry, (2) infrared radiative pumping of HCN, and (3) more HCN J=4–3 excitation. Multiple J-transition data of HCN, HCO⁺, and HNC, both at vibrational ground and excited levels, are needed to better separate these scenarios.
4. The ULIRG, IRAS 22491–1808, whose observed infrared spectral shape is explained by starburst activity, showed a high HCN-to-HCO⁺ J=4–3 flux ratio, similar to that of buried AGN-dominated ULIRGs. This ULIRG also showed remarkably high turbulent motion. Turbulence-induced heating may heat gas and dust, and enhance the HCN J=4–3 flux. Data on other ordinary starburst-dominated ULIRGs are needed to better understand the origin of the strong HCN emission in IRAS 22491–1808, and to investigate mechanisms other than AGN activity that can enhance HCN emission.
5. The vibrationally excited HCN J=4–3 ($v_2=1f$) lines were covered with our ALMA observations, but were not clearly detected in any of the four ULIRGs.
6. In addition to the targeted molecular lines, H₂S 3(2,1)–3(1,2) and CH₃CN $v=0$ 19(3)–18(3) emission lines were serendipitously detected in a few sources, demonstrating the high sensitivity of ALMA.
7. The observed HCN J=4–3 emission peak fluxes were found to be significantly smaller than those expected from thermal excitation, suggesting that the HCN J=4–3 line is sub-thermally excited even in our active galaxy sample. We need to find the best J-transition lines, with which we can separate ULIRGs hosting luminous buried AGNs from starbursts more efficiently but with sufficient reliability.

Further observations of a larger sample of well-calibrated (U)LIRGs at multiple J-transition lines are clearly necessary to confirm the trend of molecular emission line flux ratios, depending on the primary energy sources and other galaxy properties, implied from our ALMA Cycle 0 data presented in this paper, and to understand the physical origin of the observed molecular line flux ratios.

We thank the referee, Paul Ho, for his invaluable comment. We are grateful to Drs. E. Mullar, H. Nagai, and K. Saigo for their helpful advice on ALMA data analysis. M.I. is supported by Grants-in-Aid for Scientific Research (no. 23540273) and the ALMA Japan Research Grant of NAOJ Chile Observatory, NAOJ-ALMA-0001. This paper made use of the following ALMA data: ADS/JAO.ALMA#2011.0.00020.S. ALMA is a partnership of ESO (representing its member states), NSF (USA) and NINS (Japan), together with NRC (Canada) and NSC and ASIAA (Taiwan), in cooperation with the

Republic of Chile. The Joint ALMA Observatory is operated by ESO, AUI/NRAO, and NAOJ.

REFERENCES

- Aalto, S., Booth, R. S., Black, J. H., & Johansson, L. E. B. 1995, *A&A*, 300, 369
- Antonucci, R., 1993, *ARA&A*, 31, 473
- Armus, L., Charmandaris, V., Bernard-Salas, J., et al. 2007, *ApJ*, 656, 148
- Armus, L., Heckman, T. M., & Miley, G. K. 1989, *ApJ*, 347, 72
- Bardeen, J. M. 1970, *Nature*, 226, 64
- Caputi, K. I., Lagache, G., Yan, L., et al. 2007, *ApJ*, 660, 97
- Clavel, J., Schulz, B., Altieri, B., et al. 2000, *A&A*, 357, 839
- Costagliola, F., Aalto, S., Rodriguez, M. I., et al. 2011, *A&A*, 528, 30
- Costagliola, F., Aalto, S., Sakamoto, K., et al. 2013, *A&A*, 556, 66
- Dasyra, K. M., Yan, L., Helou, G., et al. 2009, *ApJ*, 701, 1123
- Donley, J. L., Rieke, G. H., Perez-Gonzalez, P. G., & Barro, G. 2008, *ApJ*, 687, 111
- Duc, P. -A., Mirabel, I. F., & Maza, J. 1997, *A&AS*, 124, 533
- Dudley, C. C., & Wynn-Williams, C. G. 1997, *ApJ*, 488, 720
- Ferrarese, L., & Merritt, D. 2000, *apJ*, 539, L9
- Gao, Y., & Solomon, P. M. 2004a, *ApJS*, 152, 63
- Gao, Y., & Solomon, P. M. 2004b, *ApJ*, 606, 271
- Goto, T., Takagi, T., Matsuhara, H., et al. 2010, *A&A*, 514, 6
- Gracia-Carpio, J., Garcia-Burillo, S., Planesas, P., Fuente, A., & Usero, A. 2008, *A&A*, 479, 703
- Gultekin, K., Richstone, D. O., Gebhardt, K., et al. 2009, *ApJ*, 698, 198
- Harada, N., Herbst, E., & Wakelam, V. 2010, *ApJ*, 721, 1570
- Harada, N., Thompson, T. A., & Herbst, E. 2013, *ApJ*, 765, 108
- Hopkins, P. F., Hernquist, L., Cox, T. J., et al. 2006, *ApJS*, 163, 1
- Imanishi, M. 2002, *ApJ*, 569, 44
- Imanishi, M. 2003, *ApJ*, 599, 918
- Imanishi, M. 2006, *AJ*, 131, 2406
- Imanishi, M. 2009, *ApJ*, 694, 751
- Imanishi, M., & Dudley, C. C. 2000, *ApJ*, 545, 701
- Imanishi, M., Dudley, C. C., & Maloney, P. R. 2006a, *ApJ*, 637, 114
- Imanishi, M., Dudley, C. C., Maiolino, R., et al. 2007a, *ApJS*, 171, 72
- Imanishi, M., Ichikawa, K., Takeuchi, T., et al. 2011b, *PASJ*, 63, S447
- Imanishi, M., Imase, K., Oi, N., & Ichikawa, K. 2011a, *AJ*, 141, 156
- Imanishi, M., Maiolino, R., & Nakagawa, T. 2010a, *ApJ*, 709, 801
- Imanishi, M., Nakagawa, T., Ohya, Y., et al. 2008, *PASJ*, 60, S489
- Imanishi, M., Nakagawa, T., Shirahata, M., Ohya, Y., & Onaka, T. 2010b, *ApJ*, 721, 1233
- Imanishi, M., & Nakanishi, K. 2006, *PASJ*, 58, 813
- Imanishi, M., & Nakanishi, K. 2013a, *AJ*, 146, 47
- Imanishi, M., & Nakanishi, K. 2013b, *AJ*, 146, 91
- Imanishi, M., Nakanishi, K., & Kohno, K. 2006b, *AJ*, 131, 2888
- Imanishi, M., Nakanishi, K., Kuno, N., & Kohno, K. 2004, *AJ*, 128, 2037
- Imanishi, M., Nakanishi, K., Tamura, Y., Oi, N., & Kohno, K. 2007b, *AJ*, 134, 2366
- Imanishi, M., Nakanishi, K., Tamura, Y., & Peng, C. -H. 2009, *AJ*, 137, 3581
- Imanishi, M., Nakanishi, K., Yamada, M., Tamura, Y., & Kohno, K. 2010c, *PASJ*, 62, 201
- Imanishi, M., & Saito, Y. 2014, *ApJ*, 780, 106
- Imanishi, M., & Wada, K. 2004, *ApJ*, 617, 214
- Iono, D., Saito, T., Yun, M. S., et al. 2013, *PASJ*, 65, L7
- Jiang, X., Wang, J., & Gu, Q., 2011, *MNRAS*, 418, 1753
- Kauffmann, G., Heckman, T. M., Tremonti, C., et al. 2003, *MNRAS*, 346, 1055
- Kewley, L. J., Heisler, C. A., Dopita, M. A., & Lumsden, S. 2001, *ApJS*, 132, 37
- Kim, D. -C., & Sanders, D. B., 1998, *ApJS*, 119, 41
- Kim, D. -C., Veilleux, S., & Sanders, D. B., 2002, *ApJS*, 143, 277
- Kohno, K. 2005, in *AIP Conf. Ser.* 783, *The Evolution of Starbursts*, ed. S. Hüttemeister, E. Manthey, D. Bomans, & K. Weis (New York: AIP), 203 (astro-ph/0508420)
- Komatsu, E., Dunkley, J., Nolte, M. R., et al. 2009, *ApJS*, 180, 330
- Krips, M., Neri, R., Garcia-Burillo, S., et al. 2008, *ApJ*, 677, 262
- Lahuis, F., Spoon, H. W. W., Tielens, A. G. G. M., et al. 2007, *ApJ*, 659, 296
- Lee, J. C., Hwang, H. S., Lee, M. G., et al. 2012, *ApJ*, 756, 95
- Lee, N., Le Floch, E., Sanders, D. B., et al. 2010, *ApJ*, 717, 175
- Lintott, C., & Viti, S. 2006, *ApJ*, 646, L37
- Magnelli, B., Elbaz, D., Chary, R. R., et al. 2011, *A&A*, 528, 35
- Magorrian, J., Tremaine, S., Richstone, D., et al. 1998, *ApJ*, 115, 2285
- Matsushita, S., Iono, D., Petitpas, G. R., et al. 2009, *ApJ*, 693, 56
- McConnell, N. J. & Ma, C-P. 2013, *ApJ*, 764, 184
- Meijerink, R., & Spaans, M. 2005, *A&A*, 436, 397
- Meijerink, R., Spaans, M., & Israel, F. P. 2007, *A&A*, 461, 793
- Murphy, E. J., Chary, R. -R., Dickinson, M., et al. 2011, *ApJ*, 732, 126
- Nakagawa, T., Matsuhara, H., & Kawakatsu, Y. 2012, *SPIE*, 8442, 0
- Nakanishi, K., Okumura, S. K., Kohno, K., Kawabe, R., & Nakagawa, T. 2005, *PASJ*, 57, 575
- Nandra, K., Iwasawa, K. 2007, *MNRAS*, 382, L1
- Nardini, E., Risaliti, G., Salvati, M., et al. 2008, *MNRAS*, 385, L130
- Nardini, E., Risaliti, G., Salvati, M., et al. 2009, *MNRAS*, 399, 1373
- Nardini, E., Risaliti, G., Watabe, Y., Salvati, M., & Sani, E. 2010, *MNRAS*, 405, 2505
- Netzer, H., Lutz, D., Schweitzer, M., et al. 2007, *ApJ*, 666, 806
- Nguyen-Q-Rieu, Jackson, J. M., Henkel, C., et al. 1992, *ApJ*, 399, 521
- Oi, N., Imanishi, M., & Imase, K. 2010, *PASJ*, 62, 1509
- Pan, L., & Padoan, P. 2009, *ApJ*, 692, 594
- Papadopoulos, P. P. 2007, *ApJ*, 656, 792
- Papovich, C., Rudnick, G., Le Floch, E., et al. 2007, *ApJ*, 668, 45
- Perez-Beaupuits, J. P., Aalto, S., & Gerebro, H. 2007, *A&A*, 476, 177
- Ranalli, P., Comastri, A., & Setti, G. 2003, *A&A*, 399, 39
- Rangwala, N., Maloney, P. R., Glenn, J., et al. 2011, *ApJ*, 743, 94
- Rodriguez-Ardila, A., & Viegas, S. M. 2003, *MNRAS*, 340, L33
- Sajina, A., Yan, L., Armus, L., et al. 2007, *ApJ*, 664, 713
- Sakamoto, K., Aalto, S., Evans, A. S., Wiedner, M., & Wilner, D. 2010, *ApJ*, 725, L228
- Sanders, D. B., Mazzarella, J. M., Kim, D. -C., Surace, J. A., & Soifer, B. T. 2003, *ApJ*, 126, 1607
- Sanders, D. B., & Mirabel, I. F. 1996, *ARA&A*, 34, 749
- Schmidt, M., & Green, R. F. 1983, *ApJ*, 269, 352
- Schweitzer, M., Lutz, D., Sturm, E., et al. 2006, *ApJ*, 649, 79
- Scoville, N. Z., Evans, A. S., Thompson, R., et al. 2000, *AJ*, 119, 991
- Shang, Z., Brotherton, M. S., Wills, B. J., et al. 2011, *ApJ*, 196, 2
- Shi, Y., et al. 2007, *ApJ*, 669, 841
- Shirahata, M., Nakagawa, T., Usuda, T., et al. 2013, *PASJ*, 65, 5
- Soifer, B. T., Sanders, D. B., Madore, B. F., et al. 1987, *ApJ*, 320, 238
- Soifer, B. T., Neugebauer, G., Matthews, K., et al. 2000, *AJ*, 119, 509
- Solomon, P. M., Rivolo, A. R., Barrett, J., & Yahil, A. 1987, *ApJ*, 319, 730
- Solomon, P. M., & Vanden Bout, P. A. 2005, *ARA&A*, 43, 677
- Spoon, H. W. W., Armus, L., Cami, J., et al. 2004, *ApJS*, 154, 184
- Spoon, H. W. W., Tielens, A. G. G. M., Armus, L., et al. 2006, *ApJ*, 638, 759
- Spoon, H. W. W., Armus, L., Marshall, J. A., et al. 2009, *ApJ*, 693, 1223
- Strauss, M. A., Huchra, J. P., Davis, M., et al. 1992, *ApJS*, 83, 29
- Thompson, T. A., Quataert, E., & Murray, N. 2005, *ApJ*, 630, 167
- Thorne, K. S. 1974, *ApJ*, 191, 507
- van der Tak, F. F. S., Black, J. H., Schoier, F. L., Jansen, D. J., & van Dishoeck, E. F. 2007, *A&A*, 468, 627
- Veilleux, S., Kim, D. -C., & Sanders, D. B. 1999, *ApJ*, 522, 113
- Veilleux, S., Kim, D. -C., Sanders, D. B., Mazzarella, J. M., & Soifer, B. T. 1995, *ApJS*, 98, 171
- Veilleux, S., & Osterbrock, D. E. 1987, *ApJS*, 63, 295
- Veilleux, S., Rupke, D. S. N., Kim, D.-C., et al. 2009, *ApJS*, 182, 628
- Watabe, Y., Kawakatu, N., & Imanishi, M. 2008, *ApJ*, 677, 895

Watabe, Y., Kawakatu, N., Imanishi, M., & Takeuchi, T. T. 2009, MNRAS, 400, 1803
Weedman, D. W., Soifer, B. T., Hao, L., et al. 2006, ApJ, 651, 101
Werner, M. W., Gatley, I., Harper, D. A., et al. 1976, ApJ, 204, 420

Woo, J-H., Kim, J. H., Imanishi, M., & Park, D. 2012, AJ, 143, 49
Yuan, T. -T., Kewley, L. J., Sanders, D. B. 2010, ApJ, 709, 884

TABLE 1
BASIC PROPERTIES OF OBSERVED LUMINOUS INFRARED GALAXIES

Object	Redshift	Scale [kpc/"]	f_{12} [Jy]	f_{25} [Jy]	f_{60} [Jy]	f_{100} [Jy]	$\log L_{\text{IR}}$ [L_{\odot}]	Optical Class	Energy Source
(1)	(2)	(3)	(4)	(5)	(6)	(7)	(8)	(9)	(10)
IRAS 08572+3915	0.058	1.1	0.32	1.70	7.43	4.59	12.1	LI ^a (Sy2 ^b)	B-AGN
IRAS 12127–1412	0.133	2.3	<0.13	0.24	1.54	1.13	12.1	LI ^a (HII ^b)	B-AGN
IRAS 00183–7111	0.327	4.7	<0.07	0.13	1.20	1.19	12.9	LI ^c	B-AGN
IRAS 20551–4250	0.043	0.84	0.28	1.91	12.78	9.95	12.0	LI(HII) ^d	B-AGN + SB
IRAS 22491–1808	0.076 ^A	1.4	0.05	0.55	5.44	4.45	12.1	HII ^{a,b}	SB only (?)
NGC 1614 (IRAS 04315–0840)	0.016	0.32	1.38	7.50	32.12	34.32	11.6	HII ^{b,e,f}	SB

NOTE. — Col.(1): Object name. Col.(2): Redshift. Col.(3): Physical scale in kpc for 1 arcsec. Cols.(4)–(7): f_{12} , f_{25} , f_{60} , and f_{100} are *IRAS* fluxes at 12 μm , 25 μm , 60 μm , and 100 μm , respectively, taken from Kim & Sanders (1998), Sanders et al. (2003), or *IRAS* faint source catalog. Col.(8): Decimal logarithm of infrared (8–1000 μm) luminosity in units of solar luminosity (L_{\odot}), calculated with $L_{\text{IR}} = 2.1 \times 10^{39} \times D(\text{Mpc})^2 \times (13.48 \times f_{12} + 5.16 \times f_{25} + 2.58 \times f_{60} + f_{100})$ [ergs s⁻¹] (Sanders & Mirabel 1996). Col.(9): Optical spectral classification. “HII”, “LI”, and “Sy2” denote HII-region, LINER, and Seyfert 2, respectively. ^a: Veilleux et al. (1999). ^b: Yuan et al. (2010). ^c: Armus et al. (1989). ^d: Duc et al. (1997). ^e: Veilleux et al. (1995). ^f: Kewley et al. (2001). Col.(10): Infrared and/or X-ray spectroscopic classification of primary energy sources. “B-AGN” and “SB” denote buried AGN and starburst, respectively. References are given in §2, Imanishi & Nakanishi (2013a), and Imanishi & Nakanishi (2013b).

^AThe redshift was estimated to be $z=0.076$ by Kim & Sanders (1998) and Soifer et al. (1987), but to be $z=0.078$ by Strauss et al. (1992). In this paper, we adopt $z=0.076$ (Kim & Sanders 1998) to be consistent to other ULIRGs in the *IRAS* 1Jy sample (Kim & Sanders 1998).

TABLE 2
LOG OF ALMA CYCLE 0 OBSERVATIONS

Object	Line	Date [UT]	Antenna Number	Baseline [m]	Exposure [min]	Bandpass	Calibrator Flux	Phase
(1)	(2)	(3)	(4)	(5)	(6)	(7)	(8)	(9)
IRAS 08572+3915	HCN/HCO ⁺	2012 October 21	22	21–384	19	3C279	Callisto	J0927+390
IRAS 12127–1412	HCN/HCO ⁺	2012 May 31 – June 1	20	21–402	26	3C279	Titan	J1130–148
		2012 December 14	24	15–402	22	3C279	Titan	J1130–148
	HNC	2012 June 1	21	21–402	42	3C279	Titan	J1130–148
	2012 November 5	23	21–375	40	3C279	Titan	J1130–148	
IRAS 00183–7111	HCN/HCO ⁺	2011 November 26–27	18	18–201	30	3C454.3	Callisto	J2157–694
		2011 November 28	14	18–201	29	3C454.3	Neptune	J2157–694
		2012 January 10	17	19–269	30	3C454.3	Neptune	J2157–694
	HNC	2012 January 13	17	19–269	30	3C454.3	Neptune	J2157–694
		2011 November 29	14	18–201	31	3C454.3	Neptune	J2157–694
		2012 January 13	17	19–269	31	3C454.3	Neptune	J2157–694
		2012 January 23	17	19–269	65	3C454.3	Neptune	J2157–694
IRAS 22491–1808	HCN/HCO ⁺	2012 October 21	20	21–384	26	3C454.3	Neptune	J2258–279
	HNC	2011 November 27 ^a	17	18–201	17	B0521–365	Callisto	J2258–279
		2012 November 7	23	21–382	17	B0521–365	Callisto	J2258–279

NOTE. — Col.(1): Object name. Col.(2): Observed molecular line. HCN and HCO⁺ J=4–3 lines were simultaneously taken. HNC J=4–3 observations were made separately. Col.(3): Observing date in UT. Col.(4): Number of antennas used for observations. Col.(5): Baseline length in meter. Minimum and maximum baseline lengths are shown. Col.(6): Net on source exposure time in min. In ALMA Cycle 0, requested sensitivity was defined, and observations were performed until this sensitivity was achieved. The net on source exposure times agree with the calculated exposure times in our ALMA Cycle 0 proposal within a factor of 2. Cols.(7), (8), and (9): Bandpass, flux, and phase calibrator for the target source, respectively.

^a The HNC data of IRAS 22491–1808 taken on 2011 November 27 were much noisier than those taken on 2012 November 7. We used only the latter data to investigate the quantities of HNC J=4–3 line and nearby continuum emission from IRAS 22491–1808, because addition of the former data resulted in larger noise.

TABLE 3
CENTRAL FREQUENCY OF INDIVIDUAL CORRELATOR SPECTRAL WINDOW

Object	Line	Frequency [GHz]
(1)	(2)	(3)
IRAS 08572+3915	HCN/HCO ⁺	335.071 (HCN), 336.989 (HCO ⁺), 347.164, 349.055
IRAS 12127-1412	HCN/HCO ⁺	312.891 (HCN), 314.858 (HCO ⁺), 300.971, 302.736
	HNC	320.062 (HNC), 308.561
IRAS 00183-7111	HCN/HCO ⁺	267.148 (HCN), 268.828 (HCO ⁺), 254.333, 252.449
	HNC	273.271 (HNC), 258.176
IRAS 22491-1808	HCN/HCO ⁺	329.466 (HCN), 331.351 (HCO ⁺), 341.543, 343.309
	HNC ^a	337.017 (HNC)

NOTE. — Col.(1): Object name. Col.(2): Observed molecular line. Col.(3): Central observed frequency of each correlator spectral window in GHz. For HCN and HCO⁺ J=4-3 observations, four spectral windows were used. For HNC J=4-3 observations, two spectral windows were used.

^a Although two spectral windows were used for the HNC observations of IRAS 22491-1808 on 2012 November 7, data of only one spectral window, containing the HNC J=4-3 emission line, were provided to us.

TABLE 4
CONTINUUM EMISSION

Object	Continuum	Flux	Peak Coordinate	rms	Beam patten
(1)	[GHz] (2)	[mJy beam ⁻¹] (3)	(RA,DEC)J2000 (4)	[mJy beam ⁻¹] (5)	[arcsec × arcsec] (°) (6)
IRAS 08572+3915 NW	a (342)	6.1 (39σ)	(09 00 25.39, +39 03 54.2)	0.16	1.8 × 1.1 (-110°)
IRAS 12127-1412 NE	a (308)	2.8 (28σ)	(12 15 19.13, -14 29 41.7)	0.10	0.6 × 0.5 (58°)
	b (314)	2.6 (20σ)	(12 15 19.13, -14 29 41.8)	0.13	0.6 × 0.5 (49°)
IRAS 00183-7111	a (261)	2.2 (26σ)	(00 20 34.70, -70 55 26.4)	0.084	2.5 × 1.2 (177°)
	b (266)	1.5 (23σ)	(00 20 34.70, -70 55 26.4)	0.067	2.2 × 1.2 (175°)
IRAS 22491-1808	a (336)	10.4 (64σ)	(22 51 49.35, -17 52 24.2)	0.16	0.6 × 0.5 (-8°)
	b (337)	10.6 (39σ)	(22 51 49.35, -17 52 24.1)	0.27	1.1 × 0.5 (99°)

NOTE. — Col.(1): Object name. Col.(2): Continuum-a or -b. Continuum-a data were taken simultaneously with HCN and HCO⁺ J=4-3 observations. Continuum-b data were taken simultaneously with HNC J=4-3 observations. The central frequency in GHz is added in parentheses. Col.(3): Flux in [mJy beam⁻¹] at the emission peak. Detection significance relative to the rms noise (1σ) is shown in parentheses. The rms noise level is derived from the standard deviation of sky signals in individual continuum maps. We did not include possible systematic uncertainty, which is difficult to quantify. Col.(4): The coordinate of the continuum emission peak in J2000. For reference, the near-infrared *K*-band (2.2μm) continuum emission peaks in J2000 are (09 00 25.44, +39 03 55.0) for IRAS 08572+3915 (NW nucleus), (12 15 19.14, -14 29 41.4) for IRAS 12127-1412 (NE nucleus), (22 51 49.30, -17 52 22.5) for IRAS 22491-1808 (E nucleus) (Kim et al. 2002). Col.(5): rms noise (1σ) level in [mJy beam⁻¹], estimated from the standard deviation of sky signals. Col.(6): Beam size in [arcsec × arcsec] and position angle. Position angle is 0° along the north-south direction, and increases counterclockwise.

TABLE 5
MOLECULAR LINE FLUX

Object	Line	Integrated intensity (moment 0) map				Velocity [km s ⁻¹]	Gaussian line fit		Flux [Jy km s ⁻¹]
		Peak [Jy beam ⁻¹ km s ⁻¹]	rms Sum	Beam [" × "'] (°)	Peak [mJy]		FWHM [km s ⁻¹]		
(1)	(2)	(3)	(4)	(5)	(6)	(7)	(8)	(9)	(10)
IRAS 08572+3915	HCN J=4-3	2.8 (18σ)	0.15	23	1.8 × 1.1 (-113°)	17501±10	9.7±0.6	330±21	3.2±0.3
	HCO ⁺ J=4-3	3.5 (29σ)	0.12	19	2.5 × 1.1 (-111°)	17489±7	14±0.8	290±17	4.2±0.3
	H ₂ S	1.2 (4.5σ)	0.26	39	2.1 × 1.1 (-108°)	17494±41	2.4±0.3	520±99	1.3±0.3
IRAS 12127-1412	HCN J=4-3	1.1 (8.7σ)	0.12	40	0.6 × 0.5 (59°)	39924±32	2.2±0.2	570±78	1.2±0.2
	HCO ⁺ J=4-3	0.56 (5.2σ)	0.11	30	0.6 × 0.5 (59°)	39985±42	1.5±0.2	570±110	0.77±0.19
	CS J=7-6	<0.34 (<3σ)	0.11	36	0.6 × 0.5 (40°)	39869±73	1.1±0.5	240 (fix)	0.26±0.11
	HNC J=4-3	0.81 (5.3σ)	0.15	39	0.6 × 0.5 (31°)	40039±43	2.0±0.4	480±86	0.91±0.23
	CH ₃ CN	0.35 (5.1σ)	0.068	31	0.6 × 0.5 (62°)	39984±95	0.7±0.3	480 (fix)	0.30±0.12
IRAS 00183-7111	HCN J=4-3	0.70 (3.9σ)	0.18	41	2.4 × 1.2 (177°)	98576±100	1.6±0.6	620±230	0.78±0.42
	HCO ⁺ J=4-3	0.57 (3.3σ)	0.17	42	2.3 × 1.2 (177°)	98423±209	1.1±0.4	620 (fix)	0.55±0.21
	HNC J=4-3	0.40 (3.6σ)	0.11	47	2.2 × 1.2 (173°)	98216±173	0.77±0.19	620 (fix)	0.39±0.10
IRAS 22491-1808	HCN J=4-3	7.1 (38σ)	0.19	34	0.6 × 0.6 (29°)	23297±9	18±1	420±21	7.6±0.5
	HCO ⁺ J=4-3	4.7 (31σ)	0.15	42	0.6 × 0.5 (-6°)	23296±16	9.4±0.5	570±35	5.4±0.4
	H ₂ S	2.3 (26σ)	0.09	21	0.6 × 0.5 (-12°)	23275±22	9.7±0.4	360±44	3.5±0.5
	HNC J=4-3	6.5 (39σ)	0.17	33	1.1 × 0.5 (99°)	23298±5	21±1	340±11	7.2±0.3

NOTE. — Col.(1): Object name. Col.(2): Observed molecular line. HCN, HCO⁺, H₂S, and CS lines were observed simultaneously with continuum-a. HNC and CH₃CN lines were taken at the same time as continuum-b. Col.(3): Rest-frame frequency of each molecular line in [GHz]. Col.(4): Integrated intensity in [Jy beam⁻¹ km s⁻¹] at the emission peak. Detection significance relative to the rms noise (1σ) in the moment 0 map is shown in parentheses. Col.(5): rms noise (1σ) level in the moment 0 map in [Jy beam⁻¹ km s⁻¹], derived from the standard deviation of sky signals in each moment 0 map. Col.(6): The number of spectral elements summed to create moment 0 maps. Each spectral element (~19.5 MHz width) consists of 40 correlator channels binning (see §3). Col.(7): Beam size in [arcsec × arcsec] and position angle. Position angle is 0° along the north-south direction, and increases counterclockwise. Cols.(8)–(11): Gaussian fits of emission lines in the spectra at the continuum peak position, within the beam size. Col.(8): Optical velocity (v_{opt}) of emission peak in [km s⁻¹]. Col.(9): Peak flux in [mJy]. Col.(10): Observed FWHM in [km s⁻¹] in the right panels of Figures 3–6. Col.(11): Flux in [Jy km s⁻¹]. The observed FWHM in [km s⁻¹] in column 10 is divided by (1 + z) to obtain the intrinsic FWHM in [km s⁻¹].

TABLE 6
MOLECULAR LINE LUMINOSITY

Object	Line	ν _{rest} [GHz]	Luminosity	
			[10 ⁴ L _⊙]	[10 ⁷ K km s ⁻¹ pc ²]
(1)	(2)	(3)	(4)	(5)
IRAS 08572+3915 NW	HCN J=4-3	354.505	7.3±0.7	5.1±0.5
	HCO ⁺ J=4-3	356.734	9.7±0.7	6.6±0.5
	H ₂ S	369.101	3.1±0.7	1.9±0.4
IRAS 12127-1412 NE	HCN J=4-3	354.505	15±3	11±2
	HCO ⁺ J=4-3	356.734	9.6±2.4	6.6±1.6
	CS J=7-6	342.883	3.1±1.3	2.5±1.0
	HNC J=4-3	362.630	12±3	7.6±2.2
	CH ₃ CN	349.393	3.7±1.5	2.7±1.1
IRAS 00183-7111	HCN J=4-3	354.505	63±34	44±24
	HCO ⁺ J=4-3	356.734	45±17	31±12
	HNC J=4-3	362.630	32±8	21±5
IRAS 22491-1808	HCN J=4-3	354.505	30±2	21±1
	HCO ⁺ J=4-3	356.734	22±2	15±1
	H ₂ S	369.101	14±2	9.0±1.3
	HNC J=4-3	362.630	29±1	19±1
IRAS 20551-4250	HCN J=4-3	354.505	11±1	8.0±0.2
	HCO ⁺ J=4-3	356.734	17±1	12±1
	H ₂ S	369.101	4.1±0.2	2.5±0.2
	HNC J=4-3	362.630	7.1±0.2	4.6±0.2
	CH ₃ CN	349.393	5.2±0.2	3.8±0.2
	HCN ν ₂ =1f J=4-3	356.256	0.5±0.1	0.3±0.1

NOTE. — Col.(1): Object name. IRAS 20551-4250 is included, because molecular line luminosity information is not shown in Imanishi & Nakanishi (2013b). Col.(2): Observed molecular line. Col.(3): Rest-frame frequency of each molecular line in [GHz]. Col.(4): Molecular line luminosity in [10⁴ L_⊙], derived from the flux based on Gaussian fits (Table 5, column 11). Col.(5): Molecular line luminosity in [10⁷ K km s⁻¹ pc²], derived from the flux based on Gaussian fits (Table 5, column 11).

TABLE 7
HCN J=1–0 AND INFRARED EMISSION OF (U)LIRGS BASED ON OUR PRE-ALMA INTERFEROMETRIC DATA

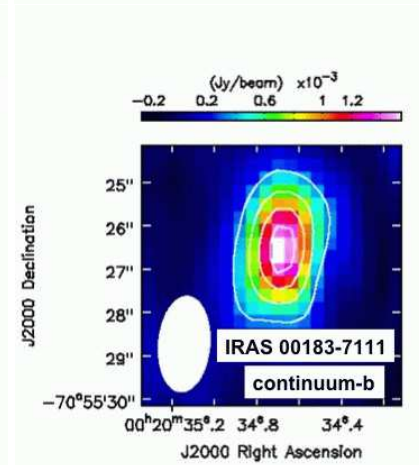
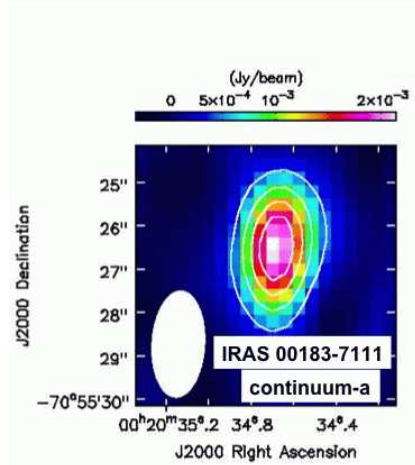
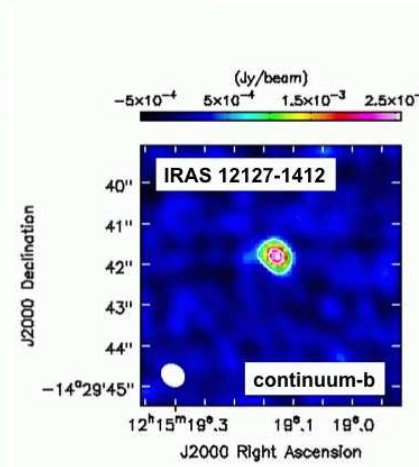
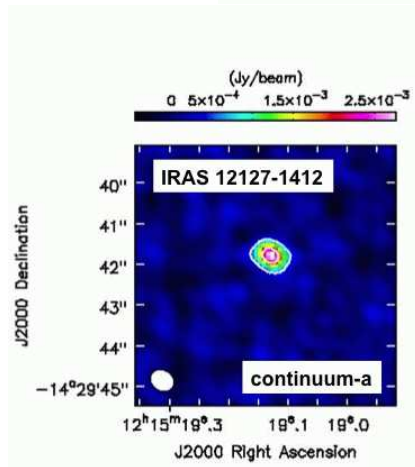
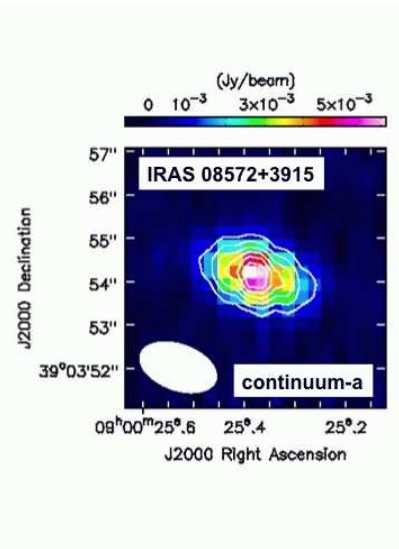
Object	Redshift	f_{IR} [$10^6 L_{\odot} \text{ Mpc}^{-2}$]	$\log L_{\text{IR}}$ [L_{\odot}]	HCN J=1–0 peak [mJy]	HCN J=1–0 flux [Jy km s $^{-1}$]	HCN J=1–0 luminosity [$10^7 \text{ K km s}^{-1} \text{ pc}^2$]
(1)	(2)	(3)	(4)	(5)	(6)	(7)
NGC 4418	0.007	8.9	11.0	40	10	3.7
UGC 5101	0.040	2.6	12.0	9	6.4	77
Mrk 273	0.038	4.2	12.2	10	4.6	50
IRAS 17208–0014	0.042	5.7	12.4	24	13	180
Arp 220	0.018	19.1	12.2	52	33	81
Mrk 231	0.042	8.2	12.5	38	10	130
IRAS 08572+3915	0.058	1.7	12.1	4	2.2	56
VV 114	0.020	5.2	11.7	15	6.9	21
He 2–10	0.003	6.1	10.1	...	6.5	0.43
NGC 2623	0.018	4.5	11.5	13	5.7	14
Mrk 266	0.028	1.7	11.5	9	2.0	12
Arp 193	0.023	3.4	11.6	27	11	42
NGC 1377	0.006	1.8	10.2	4	2.2	0.59
IC 694 (Arp 299)	0.010	14.7	11.5	24	9.9	7.2
NGC 3690 (Arp 299)	0.010	9.8	11.4	9	3.0	2.2

NOTE. — Col.(1): Object name, observed with the pre-ALMA interferometric facility, Nobeyama Millimeter Array (Imanishi et al. 2004, 2006b; Imanishi & Nakanishi 2006; Imanishi et al. 2007b, 2009). Col.(2): Redshift. Col.(3): IRAS-measured infrared (8–1000 μm) flux, calculated with $f_{\text{IR}} = 1.8 \times 10^{-14} \times (13.48 \times f_{12} + 5.16 \times f_{25} + 2.58 \times f_{60} + f_{100}) [\text{W m}^{-2}]$ (Sanders & Mirabel 1996), or equivalently $f_{\text{IR}} = 4.5 \times 10^4 \times (13.48 \times f_{12} + 5.16 \times f_{25} + 2.58 \times f_{60} + f_{100}) [10^6 L_{\odot} \text{ Mpc}^{-2}]$. Col.(4): Decimal logarithm of IRAS-measured infrared (8–1000 μm) luminosity in units of solar luminosity (L_{\odot}), calculated with $L_{\text{IR}} = 2.1 \times 10^{39} \times D(\text{Mpc})^2 \times (13.48 \times f_{12} + 5.16 \times f_{25} + 2.58 \times f_{60} + f_{100}) [\text{ergs s}^{-1}]$ (Sanders & Mirabel 1996), where we adopt $H_0 = 71 \text{ km s}^{-1} \text{ Mpc}^{-1}$, $\Omega_{\text{M}} = 0.27$, and $\Omega_{\Lambda} = 0.73$ (Komatsu et al. 2009), to estimate the luminosity distance D (Mpc) from the redshift. Col.(5): HCN J=1–0 emission peak in [mJy], based on Gaussian fit (Imanishi et al. 2004, 2006b; Imanishi & Nakanishi 2006; Imanishi et al. 2007b, 2009). Col.(6): HCN J=1–0 flux in [Jy km s $^{-1}$], based on Gaussian fit (Imanishi et al. 2004, 2006b; Imanishi & Nakanishi 2006; Imanishi et al. 2007b, 2009). Col.(7): HCN J=1–0 luminosity in [$10^7 \text{ K km s}^{-1} \text{ pc}^2$], calculated using the equation (3) of Solomon & Vanden Bout (2005).

TABLE 8
COMPARISON OF EXPECTED AND OBSERVED
HCN J=4–3 EMISSION PEAKS

Object	Expected [mJy]	Observed [mJy]
(1)	(2)	(3)
IRAS 08572+3915	~70	~10
IRAS 12127–1412	~15	~2
IRAS 00183–7111	~10	~2
IRAS 20551–4250	~110	~50
IRAS 22491–1808	~40	~20
NGC 1614	~340	~20

NOTE. — Col.(1): Object name. Col.(2): Expected HCN J=4–3 peak flux in [mJy], in the case that (a) HCN J=1–0 emission peak follows the dashed line in Figure 11 (*Left*), and (b) HCN is thermalized at up to J=4–3, where the peak flux is 16 times higher at J=4–3 than at J=1–0. Col.(3): Observed HCN J=4–3 peak flux in [mJy].



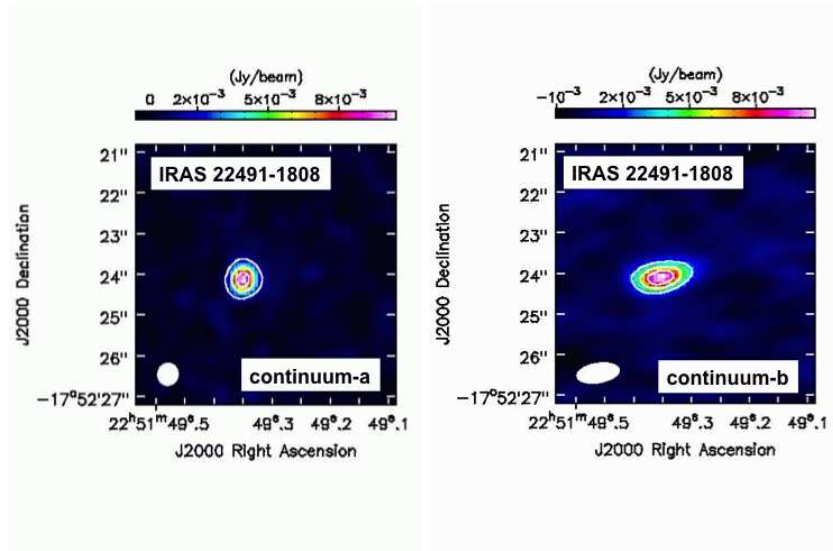


FIG. 1.— Continuum emission map. Continuum-a and -b data were taken simultaneously with HCN/HCO⁺ and HNC observations, respectively. For IRAS 08572+3915, contours are 8σ , 13σ , 18σ , 23σ , 28σ , 33σ , 38σ for continuum-a. For IRAS 12127–1412, contours are 5σ , 20σ for continuum-a, and 5σ , 15σ for continuum-b. For IRAS 00183–7111, contours are 5σ , 10σ , 15σ , 20σ for continuum-a, and 5σ , 10σ , 15σ , 20σ for continuum-b. For IRAS 22491–1808, contours are 10σ , 30σ , 50σ for continuum-a, and 10σ , 20σ , 30σ for continuum-b. The rms noise level is different in each image, and is summarized in Table 4.

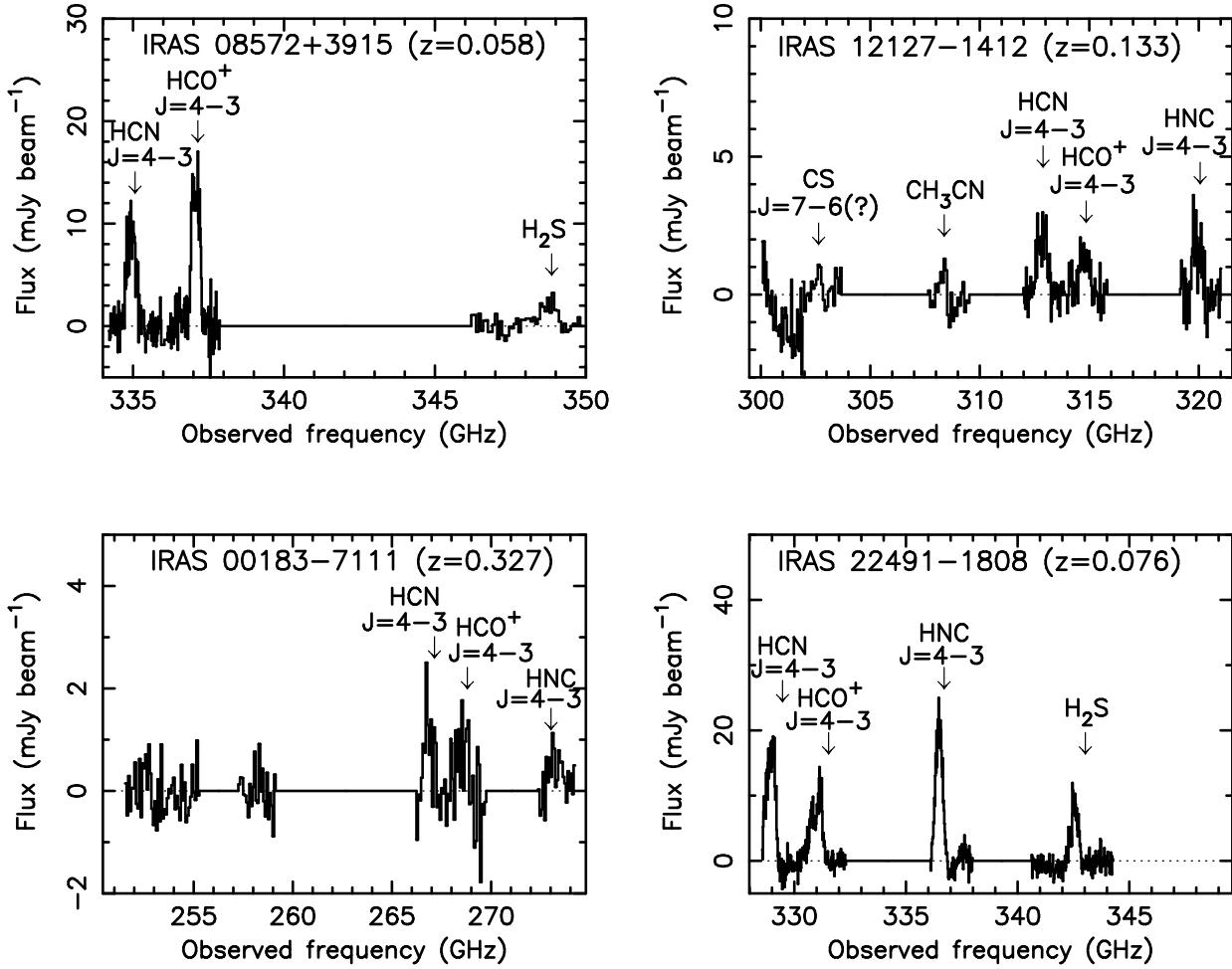


FIG. 2.— Full-frequency coverage spectra at the continuum peak position within the beam size. The abscissa shows the observed frequency in [GHz], and the ordinate shows flux in [mJy beam^{-1}]. For HCN, HCO^+ , H_2S , and CS lines, spectra are extracted at the continuum-a peak positions. For HNC and CH_3CN lines, spectra are extracted at the continuum-b peak positions. Since each spectrum was taken from two separate observations (Tables 2 and 3), actually achieved noise level is not uniform throughout the observed frequency. The expected frequencies of individual emission lines from optical redshifts are shown as downward arrows. For IRAS 22491–1808, the molecular gas emission peaks are significantly shifted to lower frequency than those expected from the adopted optical redshift of $z=0.076$ (Kim & Sanders 1998).

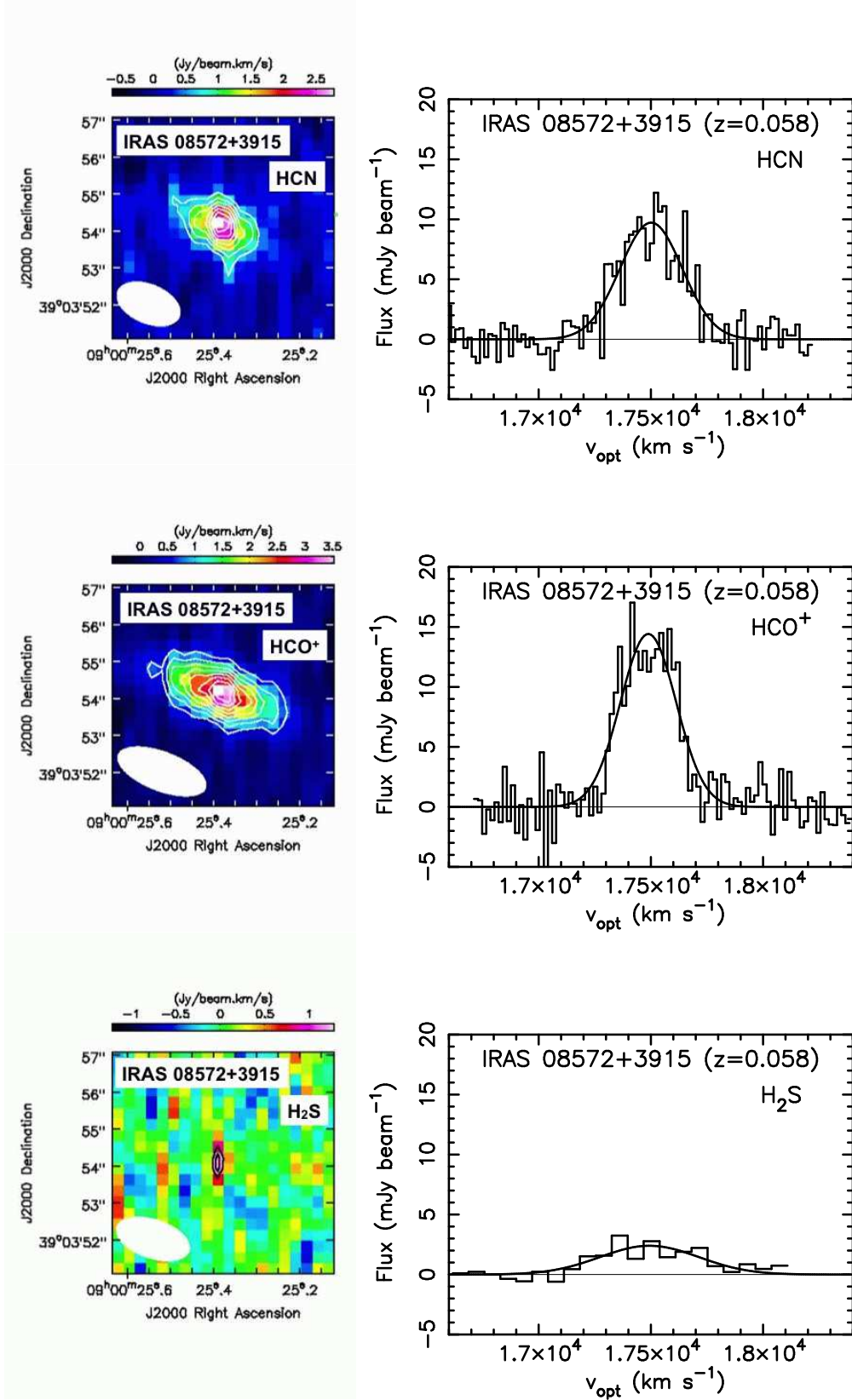
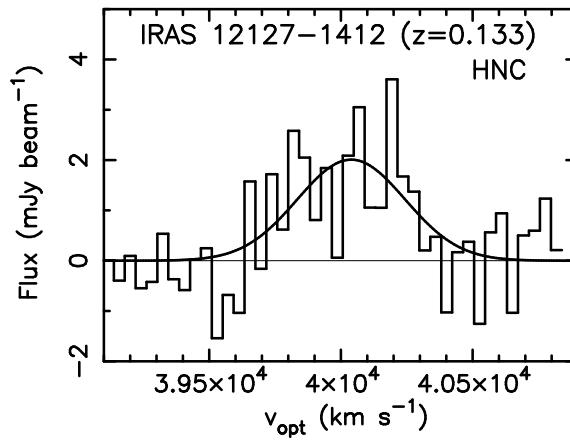
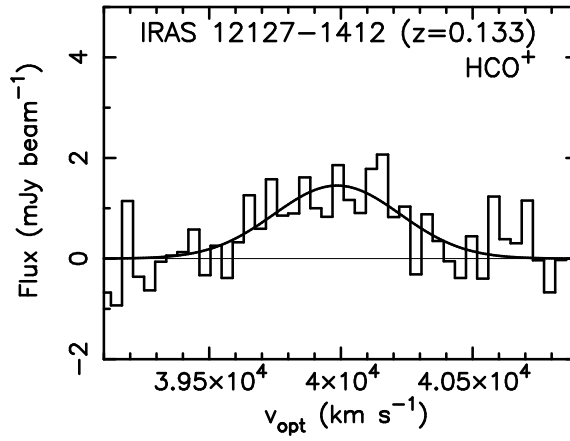
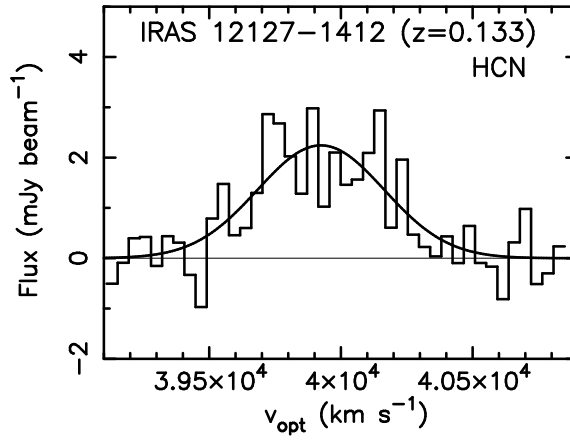
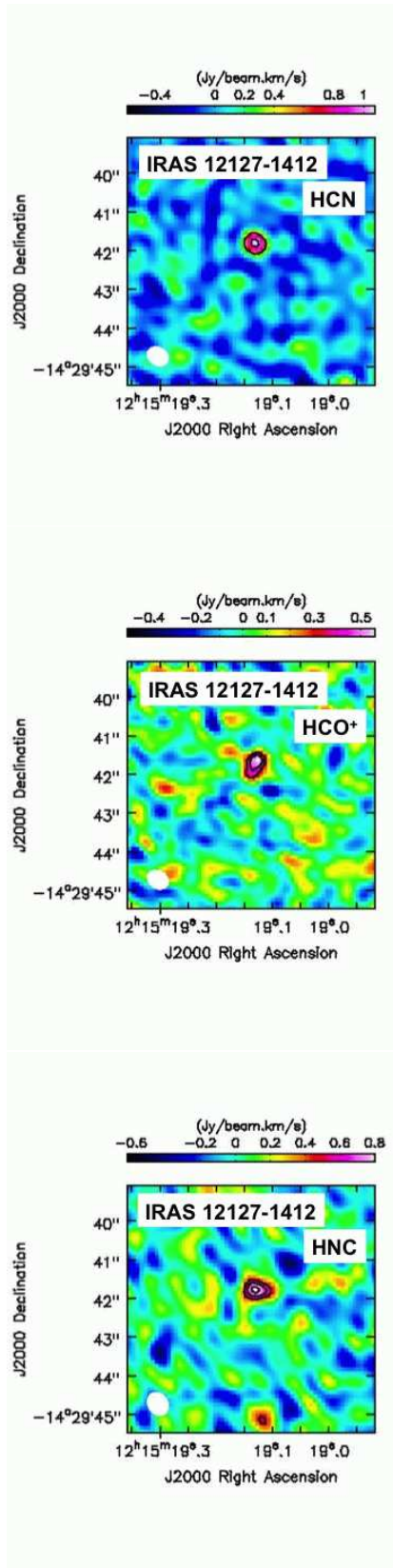


FIG. 3.— Integrated intensity (moment 0) maps (left) and spectra at the continuum peak position, within the beam size (right), of HCN, HCO⁺, and H₂S for IRAS 08572+3915. For moment 0 maps, contours are 4 σ , 6 σ , 8 σ , 10 σ , 12 σ , 14 σ , 16 σ , 18 σ , 20 σ , 23 σ , 26 σ for HCO⁺, 3 σ , 4 σ for H₂S. Detection of the H₂S emission is marginal and confirmation is required, because the signal spatial profile differs significantly from the beam pattern. For the spectra, the abscissa shows $v_{\text{opt}} \equiv c(\lambda - \lambda_0)/\lambda_0$ in [km s⁻¹], and the ordinate shows flux in [mJy beam⁻¹]. The best Gaussian fits (Table 5) are overplotted as solid curved lines. The spectrum of H₂S is shown with four spectral elements binning.



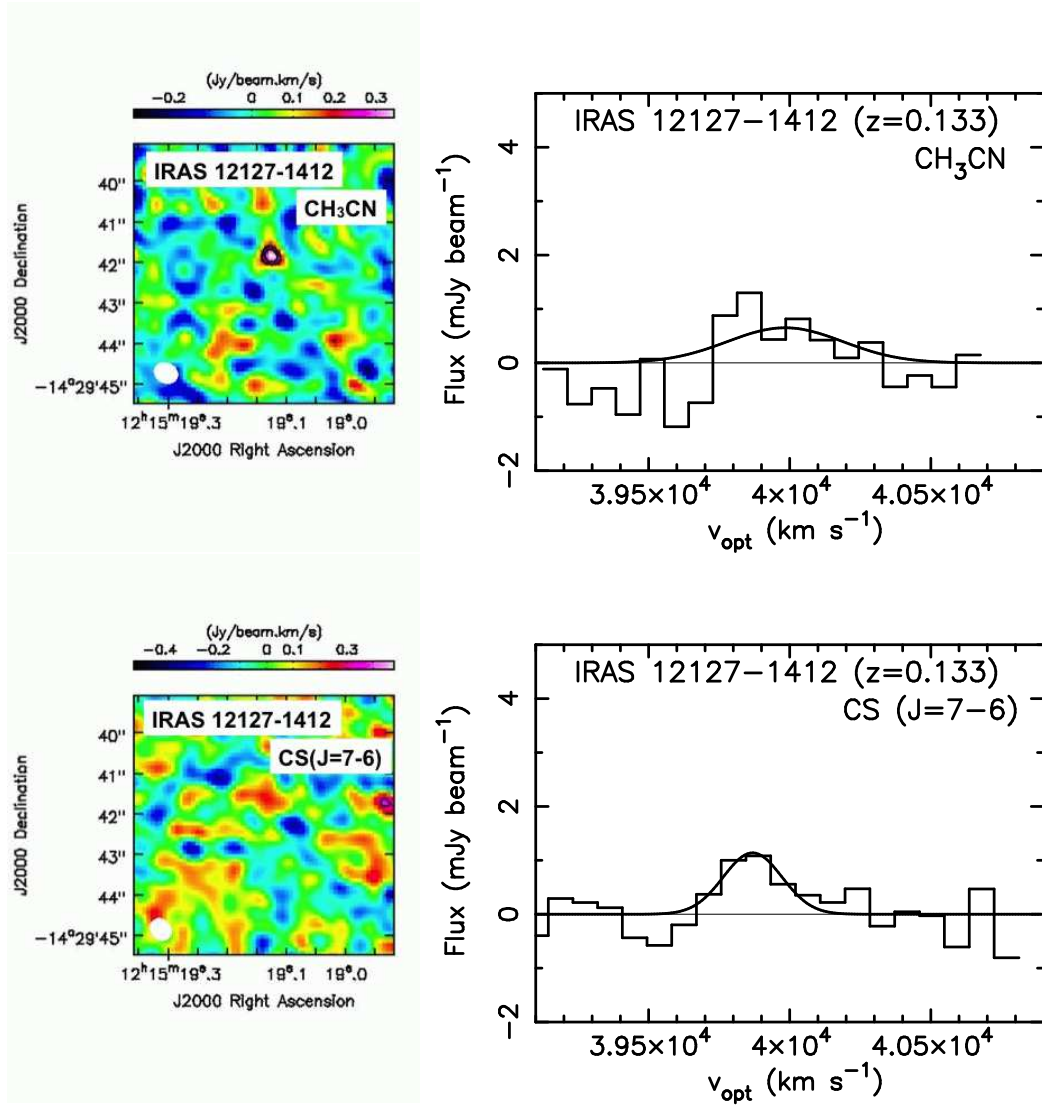


FIG. 4.— Integrated intensity (moment 0) maps (left) and spectra at the continuum peak position, within the beam size (right), of HCN, HCO⁺, HNC, CH₃CN, and CS for IRAS 12127–1412. Contours are 4 σ , 8 σ for HCN, 3 σ , 4 σ for HCO⁺, 3 σ , 4 σ , 5 σ for HNC, 3 σ , 4 σ for CH₃CN. For CS J=7–6, no emission feature with $\geq 3\sigma$ is seen. For the spectra, the abscissa shows $v_{\text{opt}} \equiv c(\lambda - \lambda_0)/\lambda_0$ in [km s⁻¹], and the ordinate shows flux in [mJy beam⁻¹]. The best Gaussian fits (Table 5) are overplotted as solid curved lines. The spectra of HCN, HCO⁺, and HNC are shown with two spectral elements binning. Those of CH₃CN and CS are shown with four spectral elements binning.

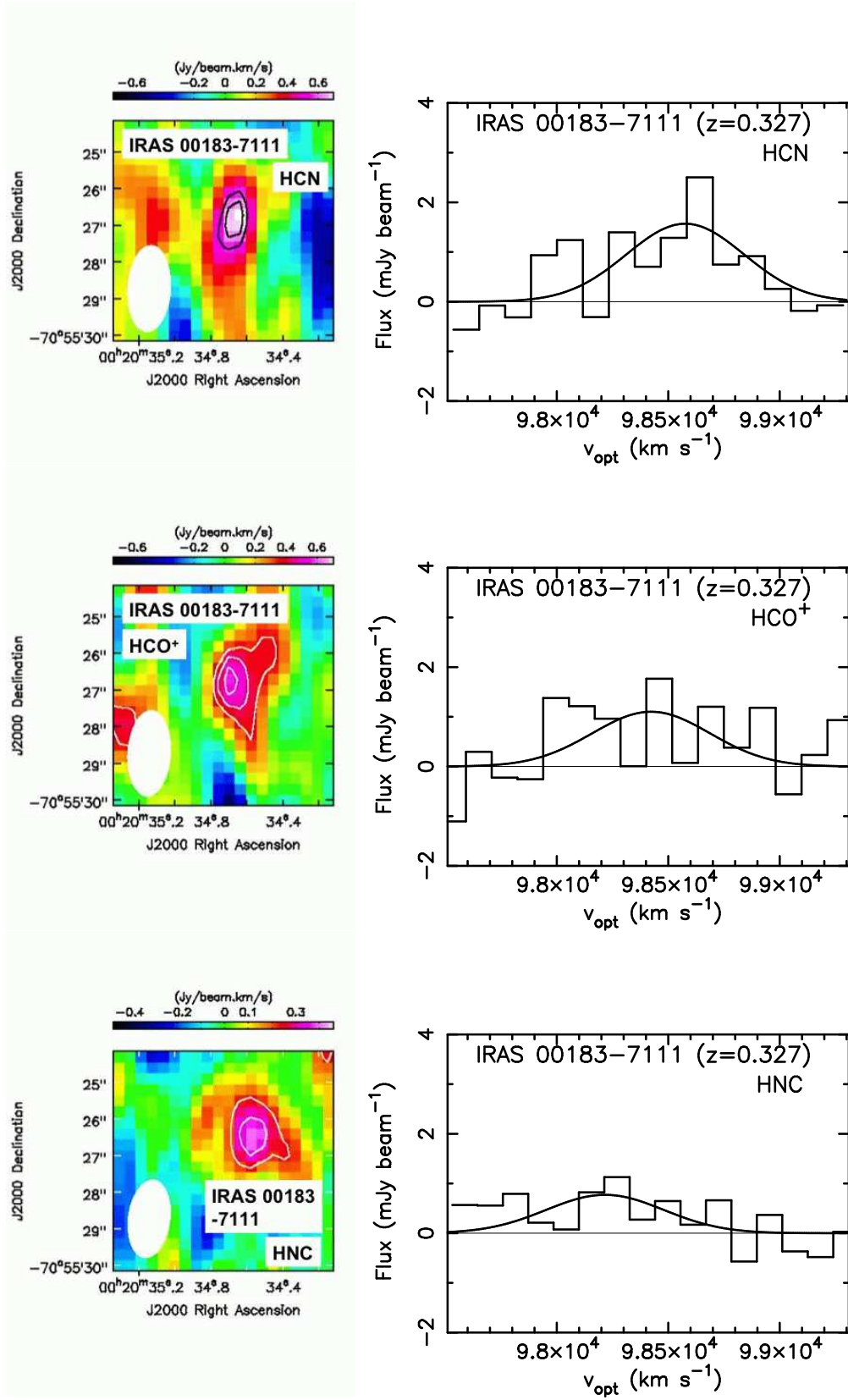
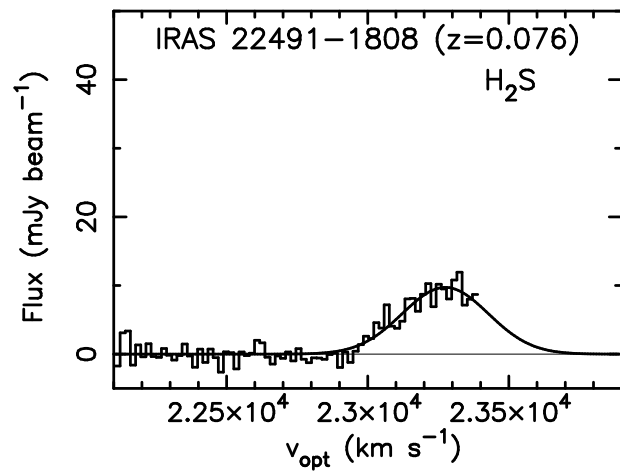
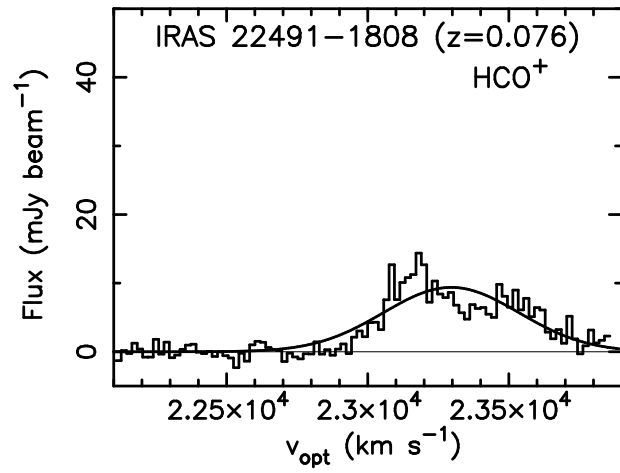
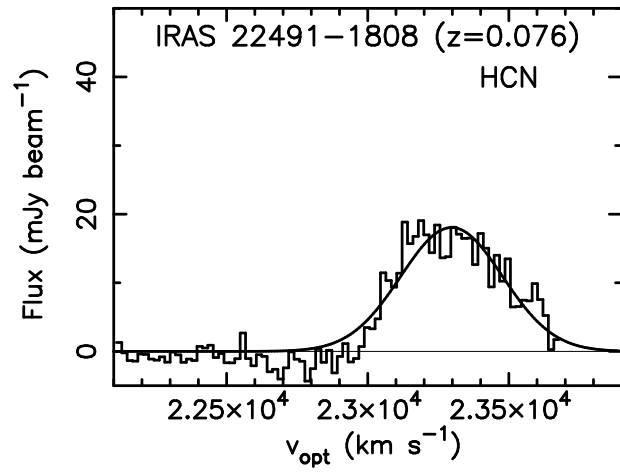
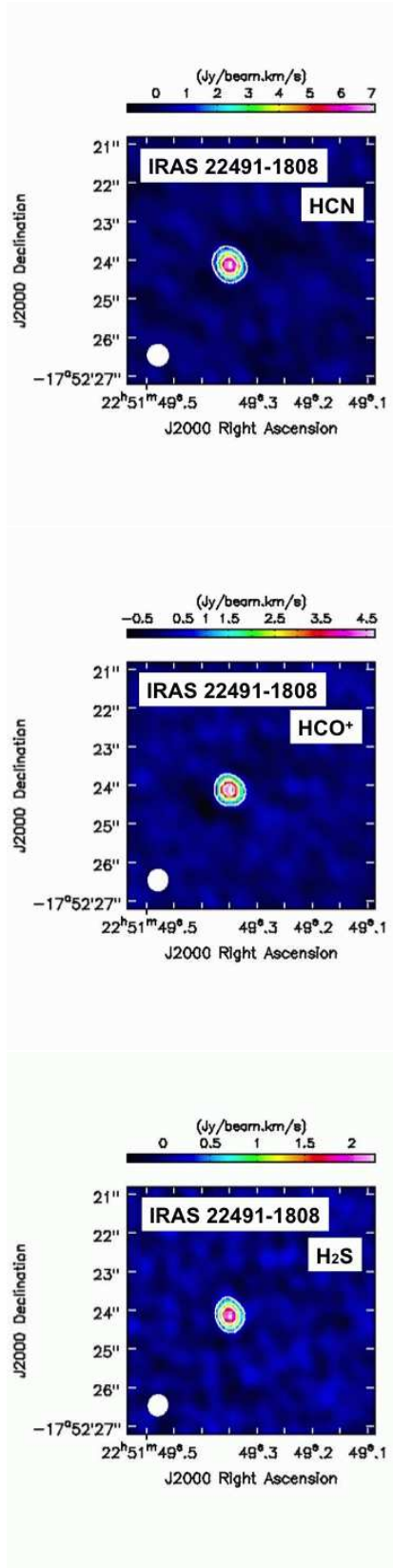


FIG. 5.— Integrated intensity (moment 0) maps (left) and spectra at the continuum peak position, within the beam size (right), of HCN, HCO⁺, and HNC for IRAS 00183–7111. Contours are 3σ , 3.5σ for HCN, 2σ , 2.5σ , 3σ for HCO⁺, 2σ , 3σ for HNC. For the spectra, the abscissa shows $v_{\text{opt}} \equiv c(\lambda - \lambda_0)/\lambda_0$ in $[\text{km s}^{-1}]$, and the ordinate shows flux in $[\text{mJy beam}^{-1}]$. The best Gaussian fits (Table 5) are overlotted as solid curved lines. Spectra are shown with four spectral elements binning.



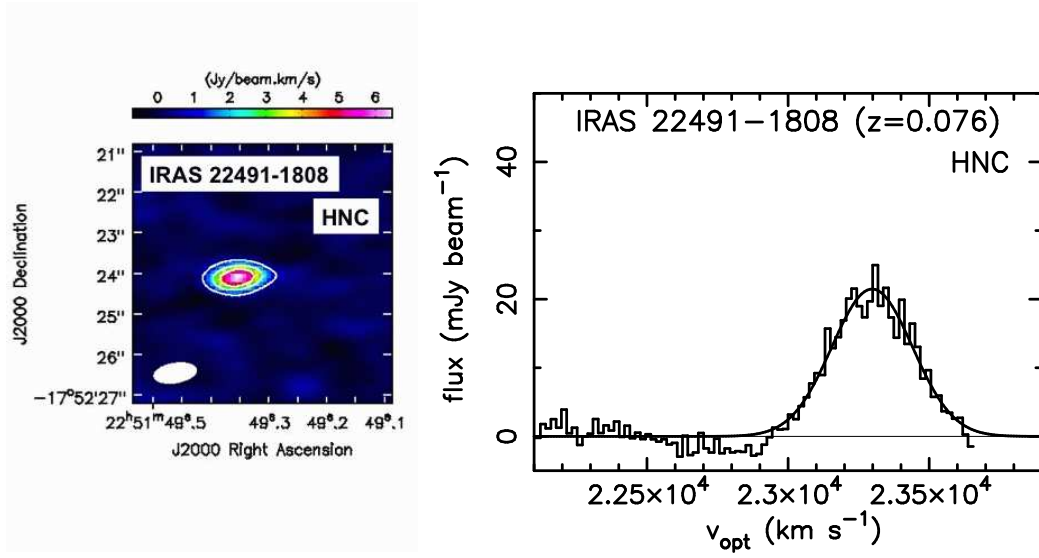


FIG. 6.— Integrated intensity (moment 0) maps (left) and spectra at the continuum peak position, within the beam size (right), of HCN, HCO⁺, H₂S, and HNC for IRAS 22491–1808. Contours are 5 σ , 15 σ , 25 σ for HCN, 5 σ , 15 σ , 25 σ for HCO⁺, 4 σ , 10 σ , 16 σ for H₂S, 5 σ , 15 σ , 25 σ for HNC. For the spectra, the abscissa shows $v_{\text{opt}} \equiv c (\lambda - \lambda_0)/\lambda_0$ in [km s⁻¹], and the ordinate shows flux in [mJy beam⁻¹]. The best Gaussian fits (Table 5) are overplotted as solid curved lines. From the optical redshift of $z = 0.076$ (Kim & Sanders 1998), the expected peak velocity is $v_{\text{opt}} \sim 22,800$ km s⁻¹. The observed peak velocities are ~ 500 km s⁻¹ higher.

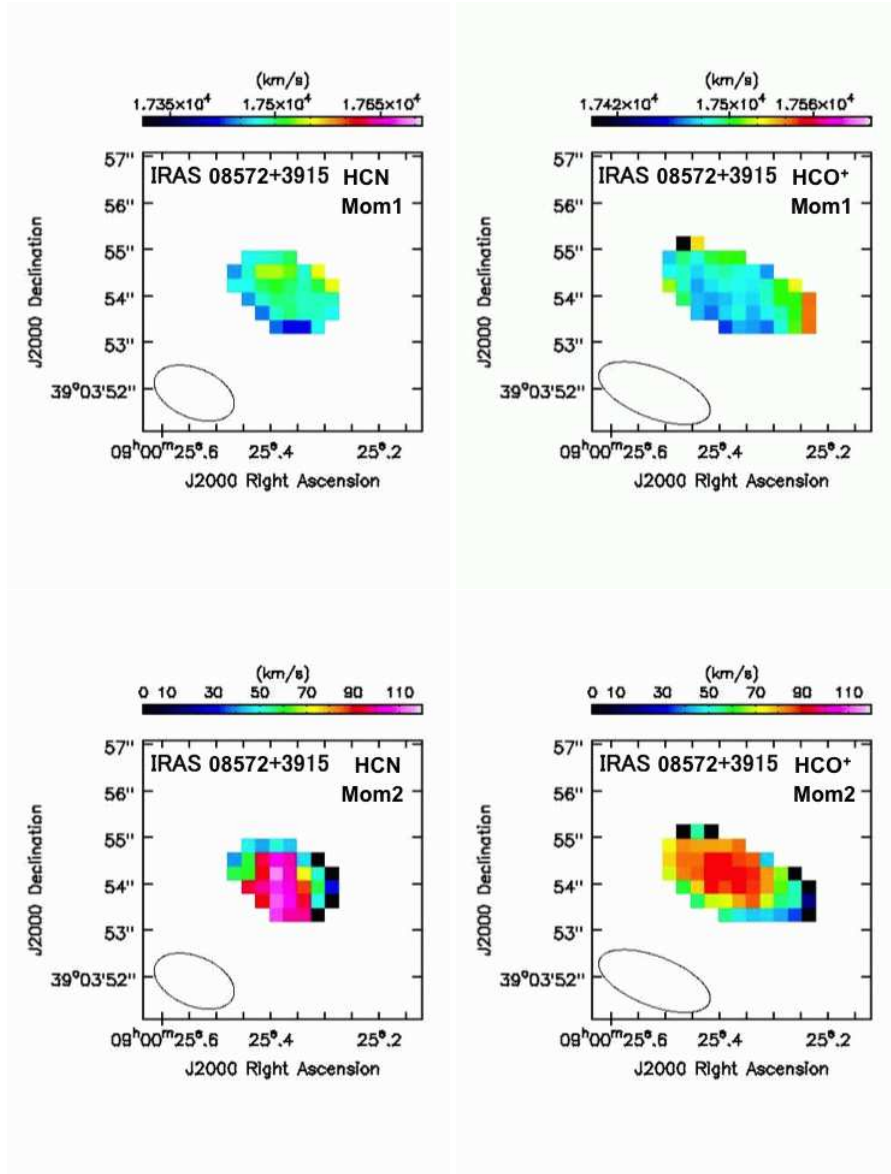


FIG. 7.— Intensity-weighted mean velocity (moment 1) and intensity-weighted velocity dispersion (moment 2) maps of HCN J=4-3 and HCO⁺ J=4-3 emission lines for IRAS 08572-3915. For moment 1 maps, the velocity is in $v_{\text{opt}} \equiv c (\lambda - \lambda_0) / \lambda_0$ in [km s⁻¹]. For moment 2 maps, the velocity is in [km s⁻¹].

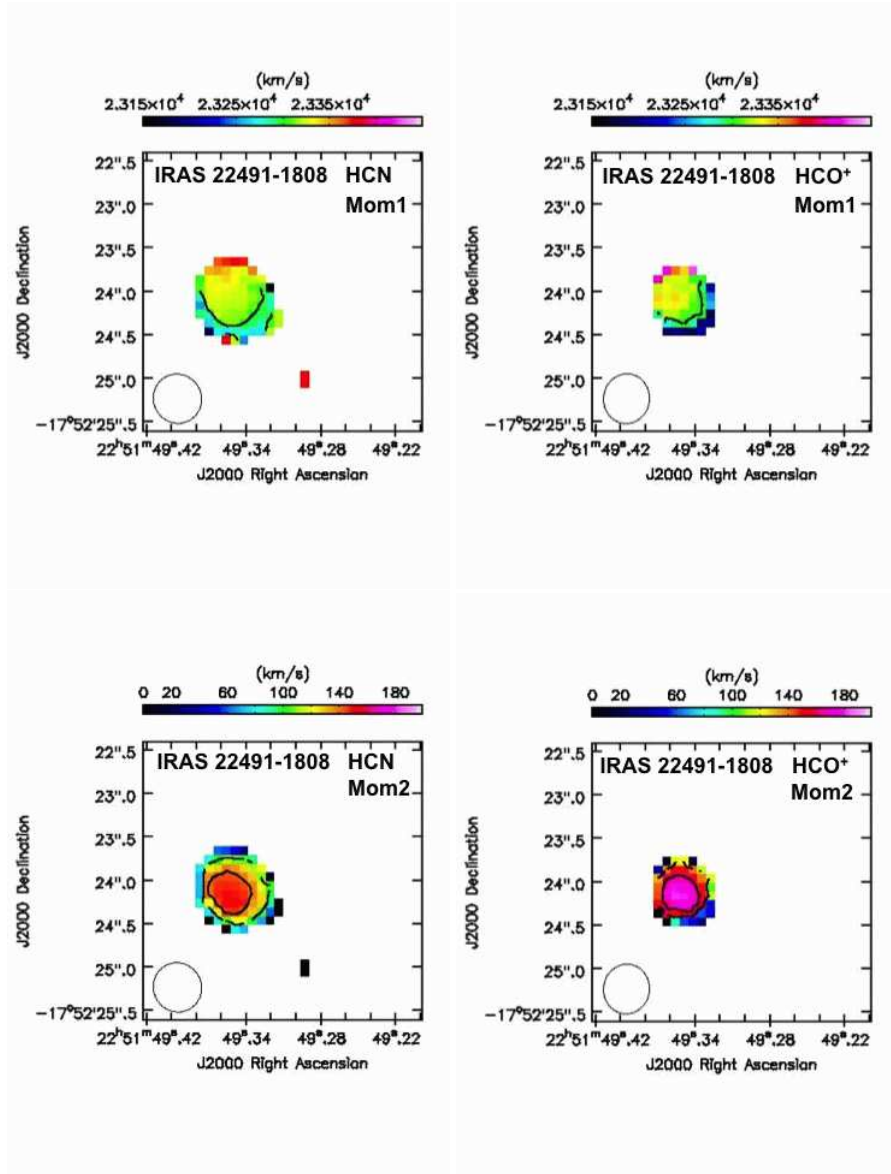


FIG. 8.— Intensity-weighted mean velocity (moment 1) and intensity-weighted velocity dispersion (moment 2) maps of HCN J=4-3 and HCO⁺ J=4-3 emission lines for IRAS 22491-1808. For moment 1 maps, the velocity is in $v_{\text{opt}} \equiv c (\lambda - \lambda_0) / \lambda_0$ in $[\text{km s}^{-1}]$. For moment 2 maps, the velocity is in $[\text{km s}^{-1}]$. The contours in moment 1 maps are 23300 km s^{-1} for both HCN and HCO⁺ J=4-3. The contours in moment 2 maps are 100 and 140 km s^{-1} for HCN J=4-3, and 120 and 160 km s^{-1} for HCO⁺ J=4-3.

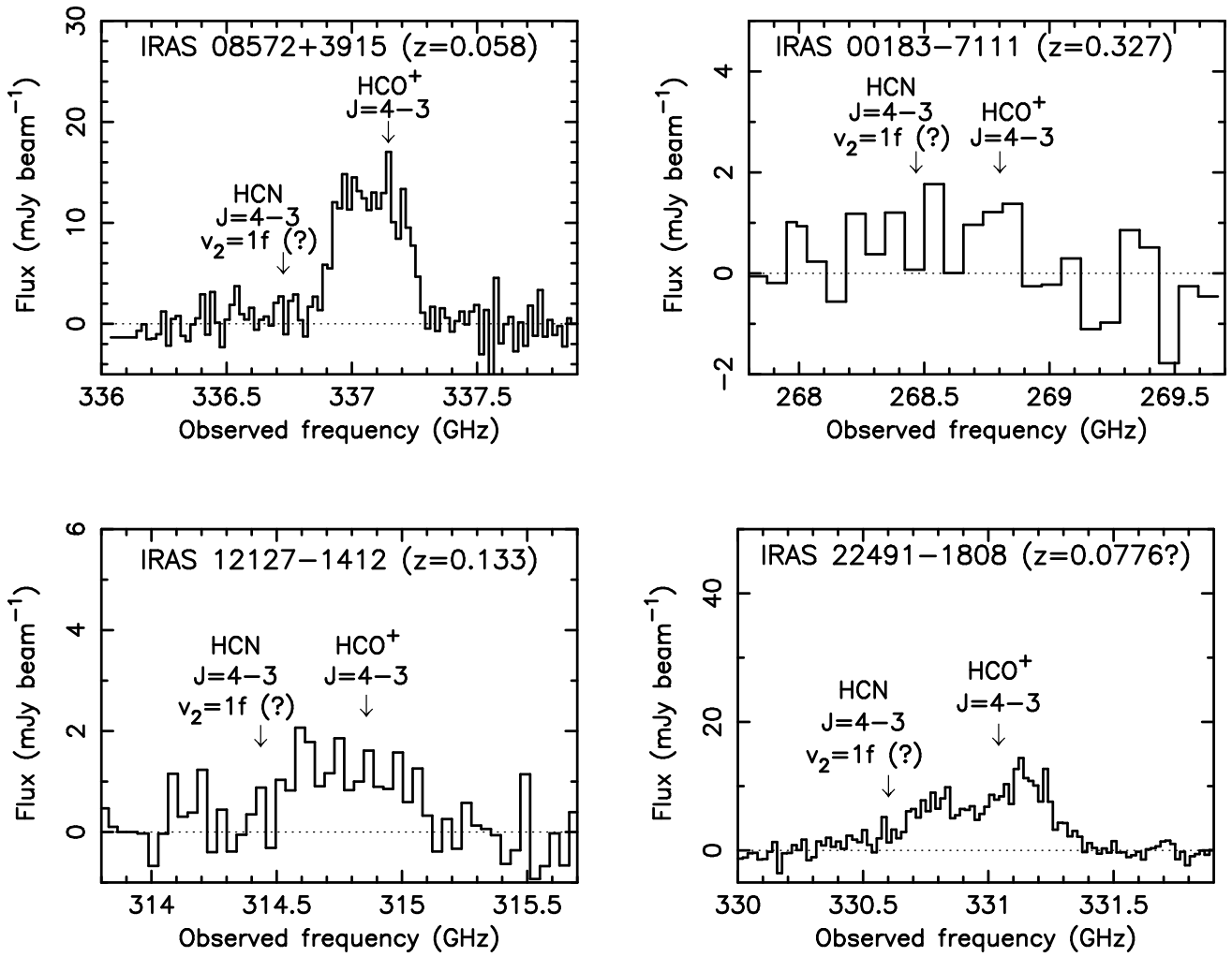


FIG. 9.— Spectra around the vibrationally excited ($v_2=1f$) HCN $J=4-3$ emission line ($\nu_{\text{rest}} = 356.256$ GHz). The abscissa shows the observed frequency in [GHz], and the ordinate shows the flux in [mJy beam⁻¹]. The expected frequencies of HCN $J=4-3$ ($v_2=1f$) and HCO⁺ $J=4-3$ ($v=0$) are shown with downward arrows. For IRAS 22491-1808, although the adopted optically derived redshift is $z = 0.076$ (Kim & Sanders 1998), we place the downward arrows at the redshift of 0.0776 derived from our ALMA data of dense molecular gas tracers.

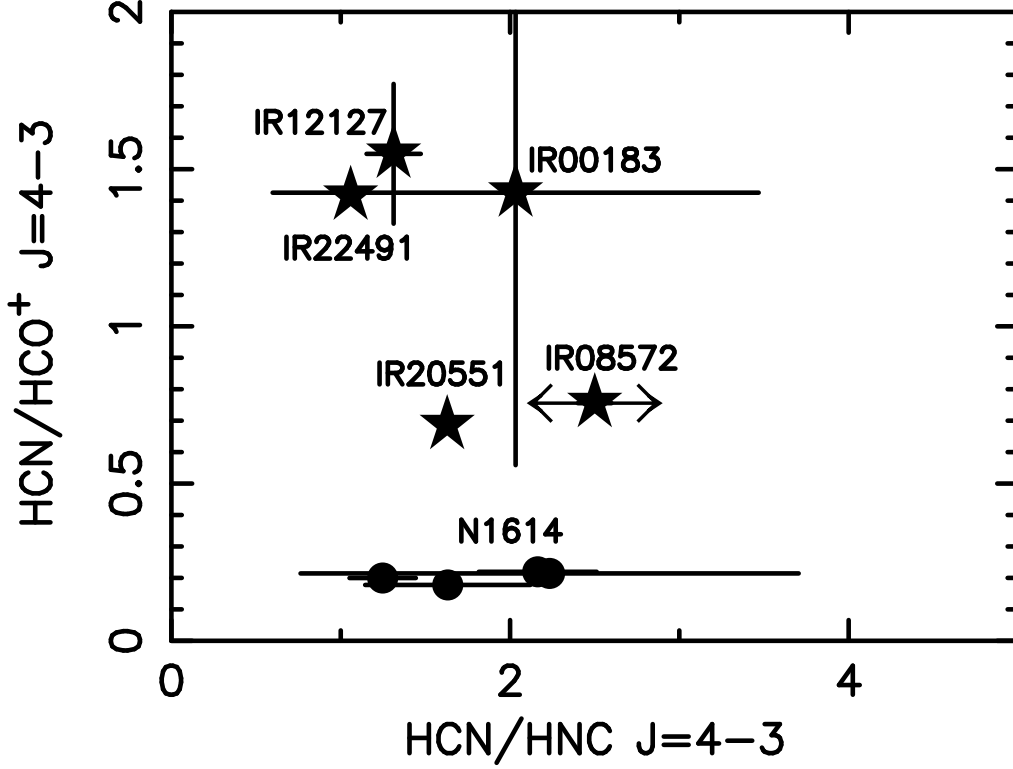


FIG. 10.— HCN-to-HNC (abscissa) and HCN-to-HCO⁺ (ordinate) flux ratios at J=4–3. The filled stars are four ULIRGs studied in this paper and IRAS 20551–4250 (Imanishi & Nakanishi 2013b). Since no HNC data are available for IRAS 08572+3915, we have no constraint on the HCN/HNC J=4–3 flux ratio. We tentatively positioned the plot at the middle of the abscissa. The filled circles are four data points of the starburst-dominated LIRG NGC 1614 (Imanishi & Nakanishi 2013a).

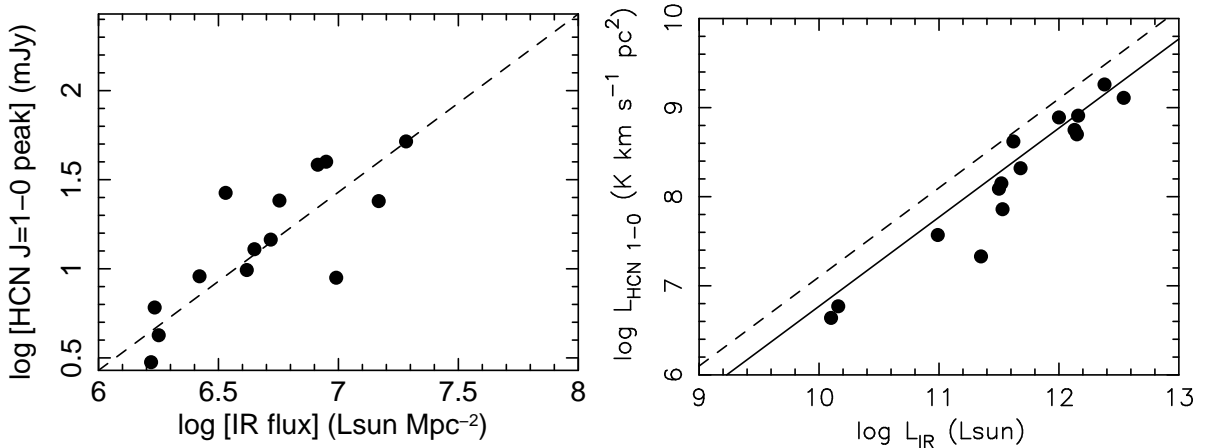


FIG. 11.— (*left*): Comparison of the decimal logarithm of the infrared flux in [$L_{\odot} \text{ Mpc}^{-2}$] from whole galactic regions measured with IRAS (abscissa) and decimal logarithm of the HCN J=1–0 *peak flux* density in [mJy] from (U)LIRG *nuclei* (ordinate), obtained from our pre-ALMA interferometric observations (Imanishi et al. 2004, 2006b; Imanishi & Nakanishi 2006; Imanishi et al. 2007b, 2009). The dashed line ($\log [\text{HCN peak}] = \log [\text{IR flux}] - 5.57$) is the ratio adopted here. (*right*): Comparison of the decimal logarithm of the infrared luminosity in [L_{\odot}] (abscissa) and decimal logarithm of the HCN J=1–0 *luminosity* in [$\text{K km s}^{-1} \text{ pc}^2$] (ordinate). The dashed line is the ratio for starburst galaxies ($\log L_{\text{HCN}} = \log L_{\text{IR}} - 2.9$) derived by Gao & Solomon (2004b). The solid line is the ratio for ULIRGs ($\log L_{\text{HCN}} = \log L_{\text{IR}} - 3.2$) estimated by Gracia-Carpio et al. (2008).